APPLIED SCIENCES AND ENGINEERING

Long-lasting comfort ocular surface drug delivery by in situ formation of an adhesive lubricative Janus nanocoating

Chuhan Wang[1,2]†, Xiaobing Liu[3,4]†, Wenyan Lv[3,4], Xiao Kuang[4], Feng Wu[4]*, Xianqun Fan[1,2]*, Yan Pang[1,2,5]*

Topical drug delivery on ocular surface always suffers from frequent administration and low bioavailability due to short drug residence. Despite advances of different adhesive ophthalmic drugs in extending release, cornea and eyelid nonselective adhesion inevitably causes ocular discomfort and even damage. Here, we describe in situ formation of an adhesive lubricative Janus nanocoating (ALJN) to enable long-lasting comfort drug delivery. By iron complexation, an asymmetric ALJN is formed on ocular surface via facile sequential instillation. The adhesive polyphenol inner layer binding with ocular surface enables drug loading and sustained release, while the lubricative zwitterionic polymer outer layer prevents eyelid adhesion to ensure comfort. Following instillation, ALJN retains on ocular surface over 24 hours and reduces blinking frequency to normal level. Moreover, ALJN demonstrates remarkable therapeutic potential in mouse and rabbit models of corneal contusion and alkali burn. This work proposes a comfortable long-lasting topical delivery platform for treating various ocular diseases.

INTRODUCTION

Ocular surface drug delivery is the most common approach to treat eye diseases (*1*). As a noninvasive and easy-to-use treatment, eye drops and eye ointment are the main modes of ocular surface topical administration (*2*). However, the presence of innate protective mechanisms in the eye—such as the corneal barrier (*3*), blinking activity, and the circulation of tears—severely hinders the permeation of dosed drugs (*4*). These factors inevitably result in short drug residence duration and the followed increasing dosage frequency. For example, more than six times per day of corticosteroids are required in the treatment of keratitis (*5*). Unfortunately, frequent administration may cause ocular surface toxicity and reduced patient compliance (*6*–*8*). To address this challenge, various drug delivery systems have been prepared for sustained drug release on ocular surface (*9*–*12*). For instance, a surface roughness–controlled cerium dioxide nanocage and a poly-L-histidine surface coating have been fabricated to prolong drug release on ocular surface (*13*). To further extend the duration of drug residence on ocular surface, a coating basing on *o*-nitrobenzaldehyde group–modified gelatin has been reported by covalently binding to corneal surface (*14*). Despite the adhesive forms of ophthalmic drugs hold promise in extending release (*15*, *16*), nonselective adhesion to both the cornea and the eyelid often obstacles eyelid movement and the deposition, splashing, and crusting around the eyelids always lead to discomfort and blurred vision (*7*). In severe cases, these issues can induce the occurrence of corneal superficial opacification (*7*). Therefore, there is an imperative need to develop noninvasive ocular drug delivery systems having prolonged ocular surface residence duration and high comfort for treating eye diseases.

In this study, we report in situ formation of an asymmetric Janus nanocoating consisting of an adhesive inner layer and a lubricative outer layer on ocular surface by facile sequential instillation (Fig. 1A). The inner layer is generated by coordinative complexation between tannic acid (TA) and the metal ions of Fe^{3+}, while the outer layer is formed via coordinative complexation between the phosphate groups of poly(2-methylpropylene glycol phosphate choline) (PMPC) and Fe^{3+} ions. Ascribed to its adhesive nature, the polyphenol inner layer is able to bind with ocular surface and provide a reservoir for drug loading and extended release. Meanwhile, the zwitterionic outer layer can avoid undesirable eyelid adhesion to acquire favorable comfort given the antifouling property of the polymer. During in vivo studies, we find that the resulting adhesive lubricative Janus nanocoating (ALJN) shows largely improved retention on ocular surface following sequential instillation, which can be prolonged up to 24 hours. ALJN is capable to reduce eye blinking frequency from 12 to 3 times/min, verifying its high comfort.

Corneal injury is one of the leading blindness causes, with approximately 6.17 million cases of visual impairment or blindness worldwide (*17*, *18*). Corneal injury is usually accompanied by structural damage, which triggers a series of events related to wound healing (*19*). Particularly, the induction of corneal inflammatory responses can cause notable reductions in corneal transparency and neovascularization as well as a variety of complications, which severely affect corneal healing and even lead to blindness (*20*). Now, clinical treatments of corneal injury mainly rely on topical ocular administration. As proof of concept, dexamethasone (DEX), an anti-inflammatory ophthalmic drug, is selected as a model drug and loaded into the inner layer of ALJN for corneal injury treatment. By virtue of the natural anti-inflammatory effect of TA and the sustained DEX release during the period of ocular surface retention, ALJN demonstrates its appealing therapeutic value toward corneal

[1]Department of Ophthalmology, Shanghai Ninth People's Hospital, School of Medicine, Shanghai Jiao Tong University, Shanghai 200011, China. [2]Shanghai Key Laboratory of Orbital Diseases and Ocular Oncology, Center for Basic Medical Research and Innovation in Visual System Diseases, Ministry of Education, Shanghai 200011, China. [3]College of Chemistry and Materials Science, Shanghai Normal University, Shanghai 200234, China. [4]Shanghai Key Laboratory for Nucleic Acid Chemistry and Nanomedicine, Institute of Molecular Medicine, State Key Laboratory of Oncogenes and Related Genes, Shanghai Cancer Institute, Renji Hospital, School of Medicine, Shanghai Jiao Tong University, Shanghai 200127, China. [5]Shanghai Frontiers Science Center of Drug Target Identification and Delivery, School of Pharmaceutical Sciences, Shanghai Jiao Tong University, Shanghai 200240, China.
*Corresponding author. Email: yanpang@sjtu.edu.cn (Y.P.); fanxq@sjtu.edu.cn (X.F.); wufeng199001@163.com (F.W.)
†These authors contributed equally to this work.

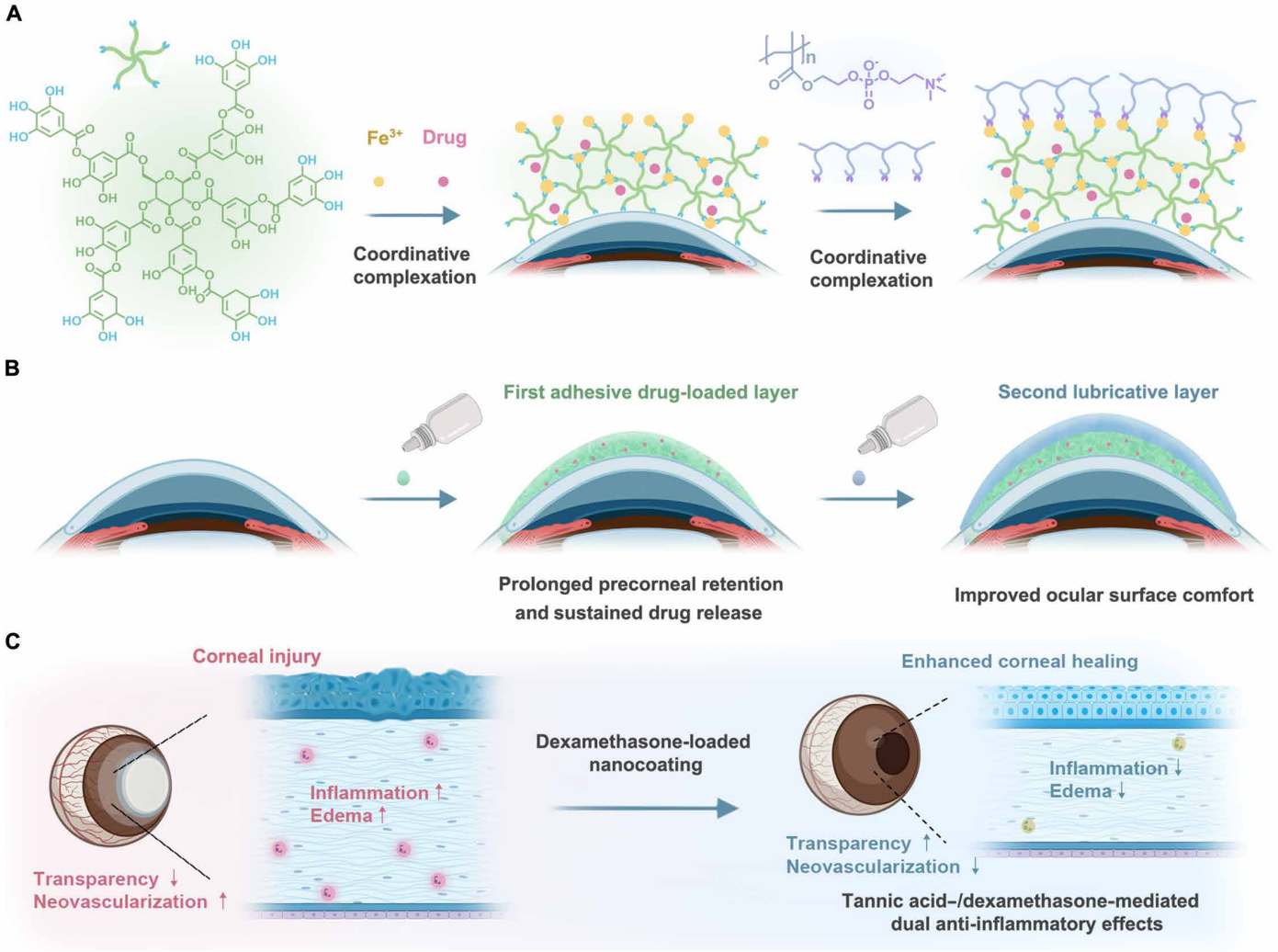

Fig. 1. Schematic illustration of the design and preparation of ALJN for long-lasting comfort ocular surface drug delivery. (**A**) Design and preparation route of ALJN. (**B**) ALJN eye drop–enabled prolonged precorneal retention, sustained drug release, and improved ocular comfort after ocular administration. (**C**) TA-/DEX-mediated dual anti-inflammatory effects of ALJN eye drops for enhanced healing of corneal injury.

injury in two models of corneal contusion and corneal alkali burn injury. Under a single-dose per day setting, ALJN exhibits superior anti-inflammatory treatment efficacies, as reflected by marked decrements in corneal haze, injury area, and neovascularization area. We anticipate that in situ formation of a Janus nanocoating can provide a versatile platform to develop topical drug delivery systems for eye disease treatment.

RESULTS

Design of ALJN

Janus structures have gained notable attention in recent years due to their ability to exhibit opposite properties on their two sides (*21*). Specifically, one side can firmly adhere to damaged tissue surfaces, while the other side that is lubricative and effectively prevents inter-tissue adhesion has gained widespread attention in recent years for tissue repair (*22*–*25*). Therefore, constructing an ocular surface coating with a Janus structure is expected to achieve long-lasting adhesion to ocular surface yet appealing lubricity to exclude eyelid adhesion after topical administration, thereby simultaneously prolonging drug residence duration and improving patient comfort. However, to the best of our knowledge, the use of Janus structures for ocular surface drug delivery has not been reported yet. This might be ascribed to that the eye is susceptible to external environments and the implementation of a Janus structure needs to be easy-to-use and highly compatible.

Polyphenols are a class of compounds with multiple tissue surface adhesion properties due to their surface-rich catechol or pyrogallol structures (*26*, *27*). TA, a commonly used polyphenol, can facilely form biocompatible TA-Fe^{3+} coatings by the multiple coordination complexations between the pyrogallol groups of TA and Fe^{3+} ions, as well as the amino and thiol groups on different tissue surfaces (*28*, *29*). Zwitterionic polymers have been widely applied in drug carriers and implant materials by virtue of their biocompatibility and antifouling feature (*30*). As a typical zwitterionic polymer, PMPC containing multiple phosphorylcholine pendent groups has

prominent interfacial lubricating effects because its hydrophilic quaternary ammonium head of phosphorylcholine can combine with surrounding water molecules to form a stable hydration layer (*31*). Note that phosphorylcholine groups are able to complex with Fe^{3+} ions (*32*), enabling on-demand formation of a PMPC-based lubricating layer on the exterior of TA-Fe^{3+} adhesive coating. Given these facts, we designed an eye drop composition that can form an asymmetric Janus nanocoating consisting of a TA-Fe^{3+} inner layer and a PMPC outer layer in situ on ocular surface via sequential instillation (Fig. 1, A to C). It is noteworthy that this nanocoating has a simple preparative procedure, and the resulting TA-Fe^{3+} inner layer not only generates a reservoir for drug encapsulation and release but also carries a natural polyphenol-based anti-inflammatory function.

Preparation and characterization of ALJN

PMPC was synthesized using a free radical polymerization, and the successful synthesis of PMPC was confirmed using proton nuclear magnetic resonance (^{1}H NMR) spectroscopy (fig. S1) and Fourier transform infrared (FTIR) spectroscopy (fig. S2). Gel permeation chromatography (GPC) measurement showed that the weight average molecular weight was 12 kDa, and the polydispersity index (PDI) was 1.43 (fig. S3). The fabrication of ALJN was accomplished using a two-step codeposition method. A transparent TA solution was mixed with a light yellow colored Fe^{3+} solution in a proportional ratio. Because of the ligand complexation between the pyrogallol groups of TA and Fe^{3+} ions, a blue-violet liquid was obtained. Following the first-step instillation, an adhesive inner single layer (SL) was formed. Owing to the rich phosphorylcholine groups, PMPC could engage in the complexation interaction with the Fe^{3+} ions in SL, resulting in a double layer (DL) structure after the second instillation. The surface morphologies of SL and DL were observed by transmission electron microscopy (TEM) (Fig. 2A) and scanning electron microscopy (SEM) (Fig. 2B), respectively. It was found that the SL surface exhibited larger and deeper pores, while the DL surface had relatively smaller and shallower pores, leading to a rougher surface of SL and a smoother surface of DL. Atomic force microscope (AFM) imaging of the corneal surface and the corneal surface after coating revealed that the average roughness of the DL surface was similar to that of the bare corneal surface but was significantly lower than that of the SL surface (Fig. 2, C and D). To measure the thickness of the layers, SL and DL were first deposited on silicon wafer surfaces and analyzed by a step profiler (fig. S4). The average thicknesses of SL and DL were observed to be 90.90 ± 36.28 nm and 151.56 ± 57.54 nm, respectively. To further measure the thickness on a more hydrophilic surface, SL and DL were formed on the surface of cornea-mimicking agar slices by drop casting (Fig. 2E), and the cross sections of the nanocoatings following freeze-drying were observed by SEM. It was found that the thicknesses of SL and DL were 201.95 ± 26.71 nm and 310.50 ± 30.04 nm, respectively (Fig. 2F). Similar to the cornea-mimicking agar surface, a comparable result was found by using mouse corneal samples (Fig. 2, G and H). It is desirable for ophthalmic formulations to maintain a thickness less than 1000 nm (*33*). Therefore, the thickness of this nanocoating could be considered moderate and would not cause extra issues by excessive thickness. In addition, compared to the ultraviolet spectrum of the Fe^{3+} ion solution, the mixture of Fe^{3+} ions and PMPC exhibited a blue shift of the absorption peak (Fig. 2I), which was attributed to the charge transfer after complexation. This result indicated that an interaction between the two components occurred, thereby forming a stable double-layered structure.

Next, we examined the drug loading of the nanocoating. DEX, a classical corticosteroid drug, was loaded by adding the DEX solution during the complexation that formed SL. Mass spectrometry confirmed the successful loading of the drug into the nanocoating, as reflected by the presence of a molecular peak $[M + H]^+$ at the mass/charge ratio (m/z) of 393.24 (Fig. 2J). Evidence for the encapsulation of DEX in the nanocoating was also verified by the FTIR spectra of SL, DEX, and SL + DEX (fig. S5). In the spectrum of drug-loaded nanocoating, stretching vibrations assigned to the carbonyl bond (−C═O) in DEX were observed at 1665 and 1604 cm^{-1}. Under different concentrations and feed ratios of Fe^{3+} ions and TA, the loading efficiency of DEX calculated by high-performance liquid chromatography (HPLC) remained constantly around 50% (Fig. 2, K and L). Therefore, we selected Fe^{3+} ions (0.8 mg/ml) and TA (5 mg/ml) with a TA-to-Fe^{3+} molar ratio of 1:1 as the preparative condition of SL layer for subsequent experiments. We then investigated the effect of varying the interval between the formation of SL and the addition of PMPC solution on the loading efficiency of DEX. As shown in fig. S6A, there was a decreasing trend as the interval time increasing from 30 to 120 s. Specifically, the loading efficiencies were calculated to be 53.58 ± 0.59%, 45.42 ± 2.12%, and 41.40 ± 60.63% for 30, 60, and 120 s, respectively. We hence chose the shortest interval time of 30 s for the addition of PMPC solution for the continuous fabrication of the nanocoating with the optimal drug-loading efficiency. In addition, the effect of varying the amount of DEX added on the loading content was studied (Fig. 2M). As expected, the quantity of loaded drug significantly increased with the feed amount of DEX increasing from 10 to 90 μg (fig. S6B). Note that in this feed range, the loading efficiency of DEX could be remained higher than 45%. Considering that the drug concentration of commercially available DEX eye drops, and the commonly dose used in ocular in vivo studies is 1 mg/ml (*34*), we used this as a reference to determine the final amount of DEX added into the nanocoating, which was 20 μg of DEX in a 20 μl of ALJN for each administration.

Lubrication, retention, and anti-inflammatory properties of ALJN in vitro

We conducted the functional validation of ALJN in vitro. First, the adhesion function of the inner layer of the nanocoating was investigated. After immersing cornea-mimicking agar slices in the SL solution, we observed that the agar slice could not slip, indicating the surface adhesion capability of the TA-Fe^{3+} inner layer (movie S1). To observe the retention performance, we piggybacked sodium fluorescein, a fluorescent indicator commonly used in ophthalmic examinations with a molecular weight close to DEX, into the nanocoating. The retention of the nanocoating was represented by the ratio of mean fluorescence intensity (MFI) after incubation in a physiological environment of phosphate-buffered saline (PBS) with gentle oscillation for different durations, with a control group using a solution of the same concentration of sodium fluorescein (Fig. 3, A and B). It was noted that due to the free form, the fluorescence intensity of the control group was higher than that of the nanocoating group at 0 hours. However, after 0.5 hours of incubation, the nanocoating group retained 93.97 ± 0.43% of the MFI, while only 22.41 ± 3.24% remained in the control group. After 4 hours of incubation, the nanocoating group maintained 90.01 ± 0.34% of the MFI. Unfortunately, the fluorescence in the control group disappeared almost completely (0.65 ± 0.78%). Even after 24 hours of incubation, the nanocoating group could retain 49.41 ± 7.80% of

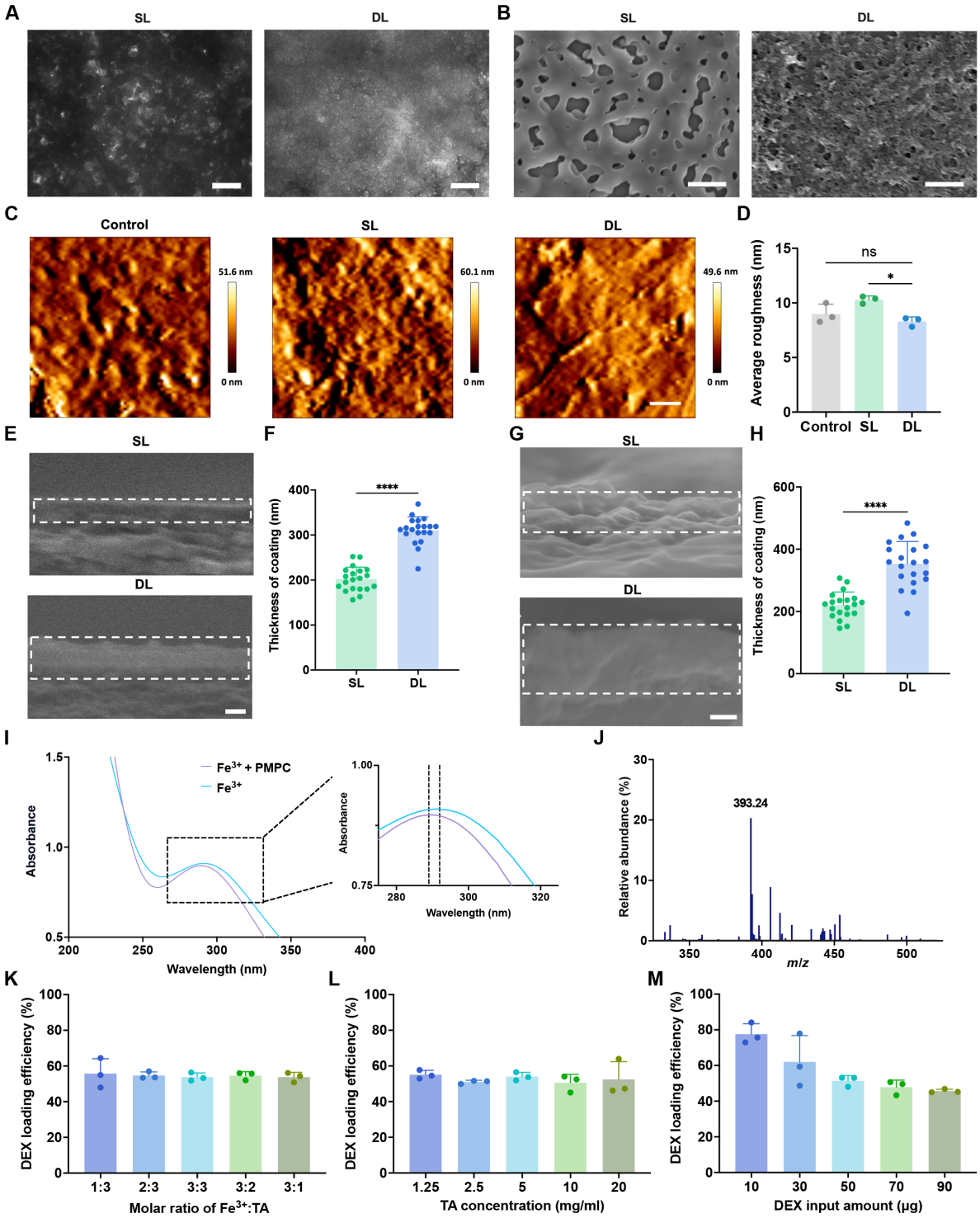

Fig. 2. Characterization of ALJN. (**A**) TEM images of the SL and DL surfaces. Scale bars, 200 nm. (**B**) SEM images of the SL and DL surfaces. Scale bars, 500 nm. (**C**) AFM images of the cornea, SL, and DL surfaces. Scale bar, 500 nm. (**D**) Average roughness of the cornea, SL, and DL surfaces ($n = 3$). (**E**) SEM images of the cross sections of SL and DL on agar slices. The dashed white box indicates the coating. Scale bar, 200 nm. (**F**) Coating thickness of SL and DL on agar slices ($n = 20$). (**G**) SEM images of the cross sections of SL and DL on cornea surface. The dashed white box indicates the coating. Scale bar, 200 nm. (**H**) Coating thickness of SL and DL on cornea surface ($n = 20$). (**I**) Ultraviolet spectra of Fe^{3+} and the mixture of Fe^{3+} and PMPC. (**J**) Mass spectrometry analysis of the drug-loaded nanocoating. *m/z*, mass/charge ratio. (**K**) Effect of the molar ratio of Fe^{3+} and TA on the drug loading efficiency of the nanocoating ($n = 3$). (**L**) Effect of coating component concentration on the drug loading efficiency of the nanocoating ($n = 3$). (**M**) Effect of the feed amount of DEX on the drug loading efficiency of the nanocoating ($n = 3$). Statistical analysis was performed using an unpaired Student's *t* test between two groups and a one-way analysis of variance (ANOVA) with Tukey's multiple comparison test for multigrouped data, giving *P* values. $^*P < 0.05$ and $^{****}P < 0.0001$. ns, no significance.

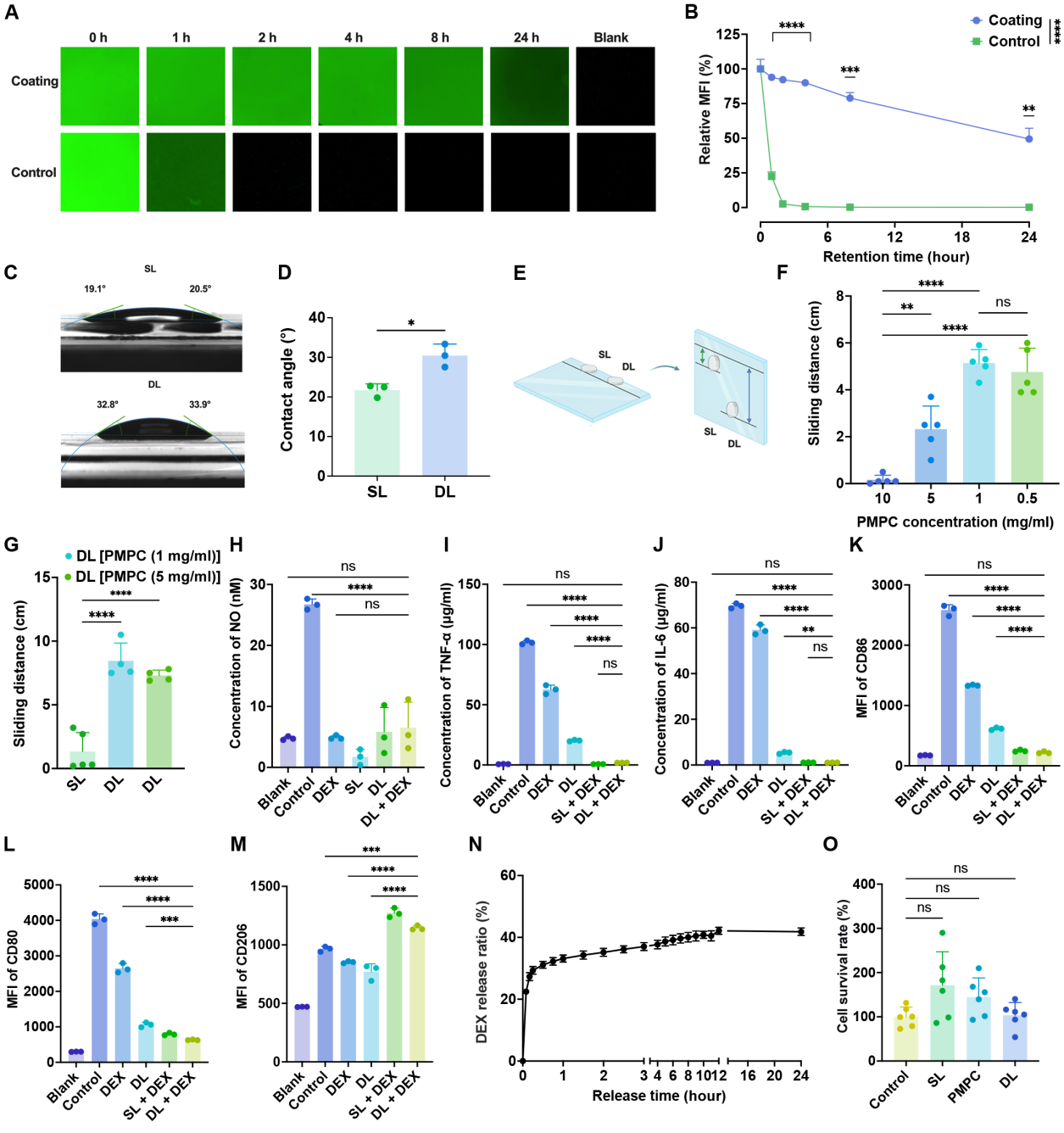

Fig. 3. In vitro functional validation of the nanocoating. (**A**) Fluorescence images of the nanocoating at specific time points in vitro. (**B**) Relative MFI of the nanocoating at specific time points ($n = 3$). (**C**) Imaging of contact angles of SL and DL. (**D**) Contact angles of SL and DL ($n = 3$). (**E**) Schematic of the sliding distance assay. (**F**) Sliding distance of agar after infiltration with PMPC ($n = 5$). (**G**) Sliding distance of agar after infiltration with SL and DL at different PMPC concentrations ($n = 4$ to 5). (**H**) Inhibitory effect of coating on the production of NO from inflammatory cells ($n = 3$). (**I** to **J**) Expression concentrations of (I) TNF-α and (J) IL-6 in macrophages ($n = 3$). (**K** to **M**) Influence of the nanocoating on the expressions of (K) CD86, (L) CD80, and (M) CD206 of macrophages ($n = 3$). (**N**) Cumulative release of DEX from the nanocoating ($n = 4$). (**O**) Effect of different coating components on cell viability ($n = 6$). Statistical analysis was performed using an unpaired Student's *t* test between two groups and a one-way ANOVA with Tukey's multiple comparison test for multigrouped data, giving *P* values. $^*P < 0.05$, $^{**}P < 0.01$, $^{***}P < 0.001$, and $^{****}P < 0.0001$. ns, no significance. h, hours.

the MFI, demonstrating its prolonged adhesion capability of over 24 hours in vitro.

To assess the interfacial lubrication effect of the PMPC layer, the contact angles of SL and DL were measured. As shown in Fig. 3 (C and D), the contact angles of SL and DL were found to be 21.68° ± 1.64° and 30.45° ± 2.90°, respectively. The increase in the contact angle indicated that DL had a higher surface tension that could result in reduced wettability and enhanced lubricity compared to SL. To quantitatively analyze the lubricity of PMPC, we measured the distance that agar slices slid on glass after being immersed in the PMPC solution with different concentrations (Fig. 3E). It was observed that at PMPC concentrations of 0.5 and 1 mg/ml, the sliding distances were 4.76 ± 1.01 cm and 5.14 ± 0.58 cm, respectively, showing a remarkable interfacial lubrication effect. However, with further increase of the PMPC concentration, there was a significant decrease in the sliding distance. As plotted in Fig. 3F, they were decreased to 2.32 ± 0.99 cm and 0.16 ± 0.19 cm at 5 and 10 mg/ml, respectively. Thus, a PMPC concentration of 1 mg/ml was chosen for the nanocoating preparation in subsequent experiments. As illustrated in fig. S7, the agar slice with a DL surface displayed a greatly improved lubricity than that of the slice with a SL surface. We further measured the lubricity of DL at different PMPC concentrations by calculating the sliding distance of the coated agar slices. Notably, the DL surface with PMPC (1 mg/ml) exhibited a sliding distance of 8.45 ± 1.40 cm, which was 6.31-fold longer than that of SL, confirming the lubricating properties of the nanocoating (Fig. 3G).

We also evaluated the anti-inflammatory effect of ALJN in vitro. The level of inflammation in macrophages, which were activated by lipopolysaccharide (LPS) to initiate the inflammatory pathway (*35*), was reflected by the production of nitric oxide (NO) after co-incubation with different components of the nanocoating (Fig. 3H). It was detected that similar to free DEX and DEX-loaded DL, the NO level after co-incubation with either SL or DL was not significantly different from that of the blank group, demonstrating the innate property of TA to suppress inflammation. Meanwhile, for the DEX-loaded SL or DL groups, the ability of macrophages to produce inflammatory cytokines tumor necrosis factor–α (TNF-α) and interleukin-6 (IL-6) upon LPS stimulation after co-incubation was also inhibited. The results showed cytokine levels comparable to the control group, which was significantly lower than those in the DL and DEX groups (Fig. 3, I and J). Similar results were observed in macrophage polarization. Flow cytometric analysis revealed that after co-incubation with DEX-loaded SL or DL, the number of $CD86^+$ and $CD80^+$ pro-inflammatory M1 macrophages decreased markedly (Fig. 3, K and L), while the number of $CD206^+$ anti-inflammatory M2 macrophages increased (Fig. 3M), confirming that the nanocoating promoted macrophage polarization toward the anti-inflammatory M2 phenotype. With loaded DEX, the nanocoating could exert a dual anti-inflammatory effect (*36*, *37*). To achieve long-lasting drug delivery, sustained release from the nanocoating was crucial. The kinetics of DEX release in PBS with gentle oscillation was investigated. As suggested in Fig. 3N, the release of DEX from the nanocoating occurred in two phases: An initial rapid release of approximately 30% of the loaded DEX within the first hour, followed by a sustained slow release over time. After an interval of 24 hours, ~45% of the encapsulated DEX was released, indicating that the drug-loaded nanocoating could release drug continuously in a long-term range. For ocular surface application, the biocompatibility of the formed coating is essential. As a result, we conducted cell biocompatibility tests on the components of the nanocoating (Fig. 3O). Cell Counting Kit-8 (CCK-8) assay results indicated that after co-incubation with SL, PMPC, or DL for 24 hours, limited adverse effects were detected against the proliferation of human corneal epithelial cells, highlighting the low cytotoxicity of the nanocoating.

Sustained retention, lubrication, and anti-inflammatory properties of ALJN in vivo

Following the functional validation of ALJN in vitro, we further validated the functionalities in vivo. To confirm the prolonged retention of the nanocoating on ocular surface, we used fluorescein as the indicator. To prevent the uptake of free fluorescein by cells, we conjugated fluorescein isothiocyanate (FITC) with TA to form TA-FITC, which was used as a component for forming the nanocoating. After instillation of the nanocoating in a form of eye drops onto the ocular surface of mice, the animals were euthanized at 0.5, 2, 4, 8, and 24 hours, respectively. Their eyes were sampled for frozen sectioning, and the presence of fluorescence on the corneal surface was observed to examine whether the nanocoating remained on the ocular surface. The control group received a FITC solution with the same fluorescence intensity. With the help of confocal imaging, we were able to observe a thin layer of green fluorescent adhering to the blue corneal tissue (Fig. 4A and fig. S8). The presence of FITC fluorescence on the ocular surface was quantitatively reflected by counting the number of mouse eyes that remained FITC fluorescence (Fig. 4B). It was found that only one mouse in the control group retained fluorescence on the ocular surface at 0.5 and 2 hours, respectively. In contrast, fluorescence was observed in all six mice in the nanocoating group at 0.5, 2, and 4 hours. Even at 24 hours after instillation, fluorescence was observed on the ocular surface of two mice, demonstrating that the nanocoating could remain on mouse ocular surface for up to 24 hours. To visually assess the biodistribution of the drug in the cornea at different time points, we substituted DEX with a fluorescent dye loaded into the nanocoating and applied it to the rabbit cornea. The corneas were harvested at specified time points for cryosectioning to examine fluorescence distribution (Fig. 4C). It was found that at 0.5 hours, the fluorescence was primarily localized in the superficial corneal layer. From 2 to 24 hours, the fluorescence spread throughout the entire cornea and then gradually decreased with time. In addition, we detected the sustained release of DEX from the coating on the rabbit ocular surface, demonstrating that the drug within the coating was gradually released over 24 hours (Fig. 4D).

To evaluate the lubricating effect of the nanocoating in vivo, we counted the number of blinks that mice performed within 5 min after ocular surface instillation of the nanocoating, as an indicator of the comfort of the eye drops (Fig. 4E). In contrast to the control group, mice showed a significantly higher average blink rate of 60.50 ± 12.29 times within 5 min after ocular surface instillation of SL. Conversely, after ocular surface instillation of DL, the average blink rate was only 16.50 ± 10.75 times within 5 min, with no significant difference compared to the control group. Furthermore, to verify whether the nanocoating could maintain its excellent lubricity under conditions of ocular surface injury, we compared the blinking frequency in mice within 5 min after the administration of the nanocoating and commercial polyvinyl alcohol eye drops (PAEDs) following corneal contusion (Fig. 4F). After injury, the mice blinked 33.17 ± 7.68 times within 5 min, which significantly reduced to 7.83 ± 2.48 blinks after applying the nanocoating, a level comparable to the 9.93 ± 4.07 blinks observed following PAED administration,

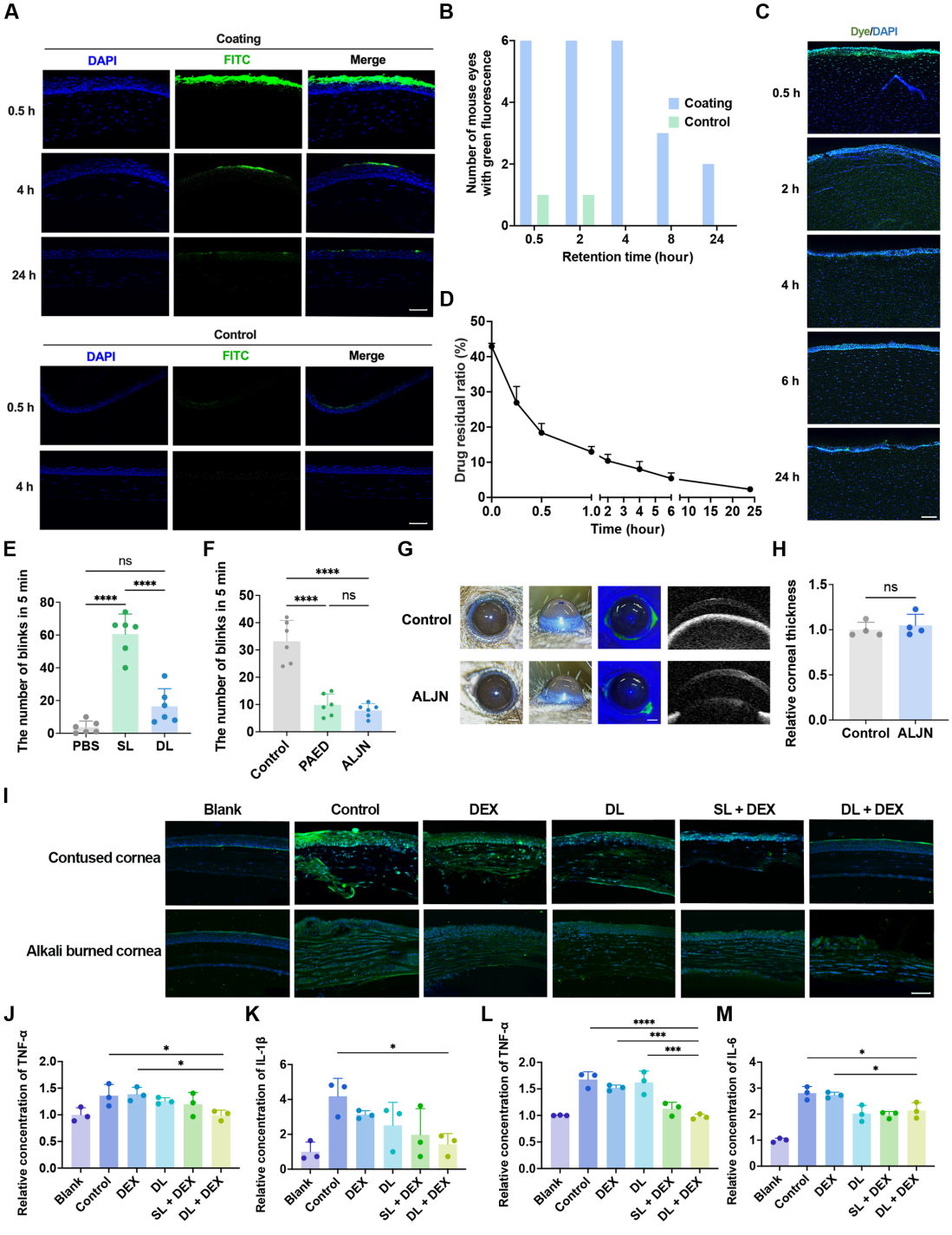

Fig. 4. In vivo functional validation of the nanocoating. (**A**) Confocal images of the nanocoating on the corneal epithelium of mice at specific time points following eye drop instillation. Blue color represents DAPI, and green color represents FITC-labeled nanocoating. Scale bars, 50 μm. (**B**) Number of mouse eyes with green florescence that was observed positive for the presence of the nanocoating at each time point. (**C**) Biodistribution of fluorescent dye in rabbit cornea at different time points. Blue color represents cell nuclei, and green color represents dye. Scale bar, 50 μm. (**D**) Drug residual ratio of DEX on rabbit ocular surface ($n = 3$). The number of blinks within 5 min following topical administration of (**E**) healthy mice and (**F**) mice with corneal contusion ($n = 6$). (**G**) Slit lamp microscopy and AS-OCT images of mice after 14 consecutive days of once-daily eye drop instillation, arranged from left to right as orthostatic views, lateral views, fluorescein sodium–stained images under a cobalt blue-filter, and OCT cross-sectional images. Scale bars, 1 μm. (**H**) Relative corneal thickness of mice after 14 days of continuous administration ($n = 4$). (**I**) Immunofluorescence staining images of corneal sections of injured cornea. Top row: Contused cornea. Bottom row: Alkali burned cornea. Scale bar, 50 μm. (**J** to **M**) Relative concentrations of (J) TNF-α and (K) IL-1β in the corneas of mice with corneal contusion and (L) TNF-α and (M) IL-6 in the corneas of mice with corneal alkali burn ($n = 3$). Statistical analysis was performed using an unpaired Student's *t* test between two groups and a one-way ANOVA with Tukey's multiple comparison test for multigrouped data, giving *P* values. $^{*}P < 0.05$, $^{***}P < 0.001$, and $^{****}P < 0.0001$. ns, no significance. h, hours.

verifying satisfactory comfort of the nanocoating. To assess the in vivo compatibility of the nanocoating, we detected the morphology of the ocular surface of mice using a slit lamp and an anterior segment optical coherence tomography (AS-OCT) after daily instillation for 5 (fig. S9) and 14 (Fig. 4, G and H) consecutive days. We observed the ocular surface under cobalt blue light after the instillation of sodium fluorescein. No abnormalities—such as morphological changes, corneal opacity, corneal neovascularization, corneal injury, and corneal thickness alterations—were observed on the ocular surface of mice after short- and long-term continuous administration, demonstrating favorable ocular surface biocompatibility of the nanocoating.

To determine the in vivo anti-inflammatory effects of the drug-loaded nanocoating, we constructed mouse models of corneal contusion and corneal alkali burn. The mice were treated with daily ocular surface eye drop instillation for several days (5 days for corneal alkali burn and 3 days for corneal contusion given the different severities of these two models). After the treatment period, the mice were euthanized, and their eyes were collected for paraffin section and immunofluorescence staining (Fig. 4I). The immunofluorescence results of TNF-α indicated that both the drug-only and nanocoating-only groups as well as the DEX-loaded SL (SL + DEX) and DEX-loaded DL (DL + DEX) groups exhibited varying degrees of TNF-α inhibition in both models. Among them, the DL + DEX group showed the strongest inhibitory effect, which was comparable to that of the blank control group. We observed that the components of the drug-loaded nanocoating had varying degrees of inhibition on TNF-α in different corneal tissues. As depicted in figs. S10 and S11, DEX was more potent to inhibit the entire corneal layer, while the nanocoating was more remarkable to suppress TNF-α in the stroma layer of the cornea. This might be attributed to differences across different corneal tissues, including cell density, the permeability and sensitivity to distinct anti-inflammatory components, the expression of relevant receptors, and the activation of inflammatory signaling pathways (*38*, *39*). In addition, we extracted corneal proteins from the eye balls after treatment and measured the levels of inflammatory factors including TNF-α, IL-1β, and IL-6 (Fig. 4, J to M). The results confirmed that the nanocoating itself had anti-inflammatory properties. Expectedly, the anti-inflammatory effect of the drug-loaded nanocoating was notably enhanced compared to that of DEX or the nanocoating alone, indicating a dual anti-inflammatory function in vivo.

Application of ALJN in treating corneal contusion

After validating prolonged retention on ocular surface, sustained drug release, lubricating properties, and anti-inflammatory capabilities of ALJN both in vitro and in vivo, we next assessed the therapeutic value of this drug delivery system in two animal models of ocular surface inflammatory diseases. Because of the exposed nature of the eye, external insults can easily cause structural and functional damage, rendering ocular trauma a common clinical condition and the leading cause of monocular blindness (*40*). Inflammation is the body's initial response to damage and infection following ocular injury, but severe inflammation can in turn lead to further damage (*41*). Therefore, inflammation control of ocular surface is a means of preventing further progression of damage and a method to promote tissue repair (*42*). In light of the ocular trauma that can be classified as mechanical and nonmechanical based on the cause of injury (*43*), we selected mouse models of corneal contusion and alkali burn injury, respectively, to explore the potential of the nanocoating in treating corneal injuries.

First, the therapeutic potential of ALJN in treating corneal mechanical injury was evaluated (Fig. 5A). A mouse model of corneal contusion was established using a corneal trephine and a corneal scraper, resulting in a relatively mild type of corneal injury. Following modeling, the corneal surface of the mice was visibly rough and uneven under light. The eye drops were administered topically to the ocular surface of mice in each group once daily for three consecutive days. The corneal condition of the mice was monitored daily using a slit lamp (Fig. 5, B to D). After 3 days of treatment, minimal changes in corneal opacity were observed in the DL + DEX group, with the surface exhibiting a very uniform reflection of light, indicating that the corneal surface was repaired effectively. In contrast, other groups exhibited different levels of corneal opacity and uneven light reflection. The corneal opacity score of the DL + DEX group (0.50 ± 0.76 points) was significantly lower than that of the DEX group (2.50 ± 1.20 points) and the control group (3.00 ± 1.07 points) (Fig. 5E). Despite the inflammation associated with corneal contusion was relatively limited and the growth of corneal neovascularization was also comparatively slow, the area of neovascularization in the corneas of mice in the DL + DEX group (1.21 ± 0.50 mm^2) was significantly lower than those in the DL group (2.54 ± 0.84 mm^2), the DEX group (3.12 ± 1.11 mm^2), and the control group (3.75 ± 0.39 mm^2) (Fig. 5F). Regarding the healing level of corneal injuries, the DL + DEX group demonstrated a promising potency (94.51 ± 6.46%), showing a significant difference compared to the DEX (70.20 ± 13.61%) and control (54.36 ± 14.73%) groups (Fig. 5G). These findings suggest that the drug-loaded DL played a substantial role in promoting the healing process of corneal injuries.

We also performed hematoxylin and eosin (H&E) staining and Masson staining on the cornea sections of mice from each group after 3 days of treatment to observe corneal morphology (Fig. 5H). Encouragingly, the corneas in the DL + DEX group exhibited a near-normal arrangement of the stroma and a regular epithelial layer, similar to that of the blank group. In other groups, varying degrees of disorganized epithelial cells or stromal edema were observed. Statistically, the corneal thickness of all coating groups differed significantly from that of the DEX and control groups (Fig. 5I), suggesting that the treatment not only addressed the immediate inflammatory response but also supported the structural integrity of the cornea. Similar results were observed in the inhibition of corneal cell infiltration (Fig. 5J), where the DL + DEX group significantly outperformed the DEX and DL groups. The results demonstrated the combined effect of the drug and the nanocoating in managing corneal injury. The notable reduction in stromal edema and epithelial disarray in the DL + DEX group indicated a more effective resolution of the pathological processes following corneal injury, which was crucial for healing and the prevention of long-term complications (*44*). In addition, the DL + DEX group showed a notable inhibitory effect on the infiltration of neutrophils in the cornea. The results of treating corneal contusion suggested that, in mild cases of corneal injury, a once-daily application of drug-loaded SL or DL nanocoating eye drops was similar effective in inhibiting acute corneal inflammation, although it was worth noting that DL + DEX with an additional lubricating ability could improve ocular surface comfort.

Application of ALJN in treating corneal alkali burn

Next, we further constructed a more severe and urgent corneal injury model, that is, corneal alkali burn injury, to evaluate the therapeutic

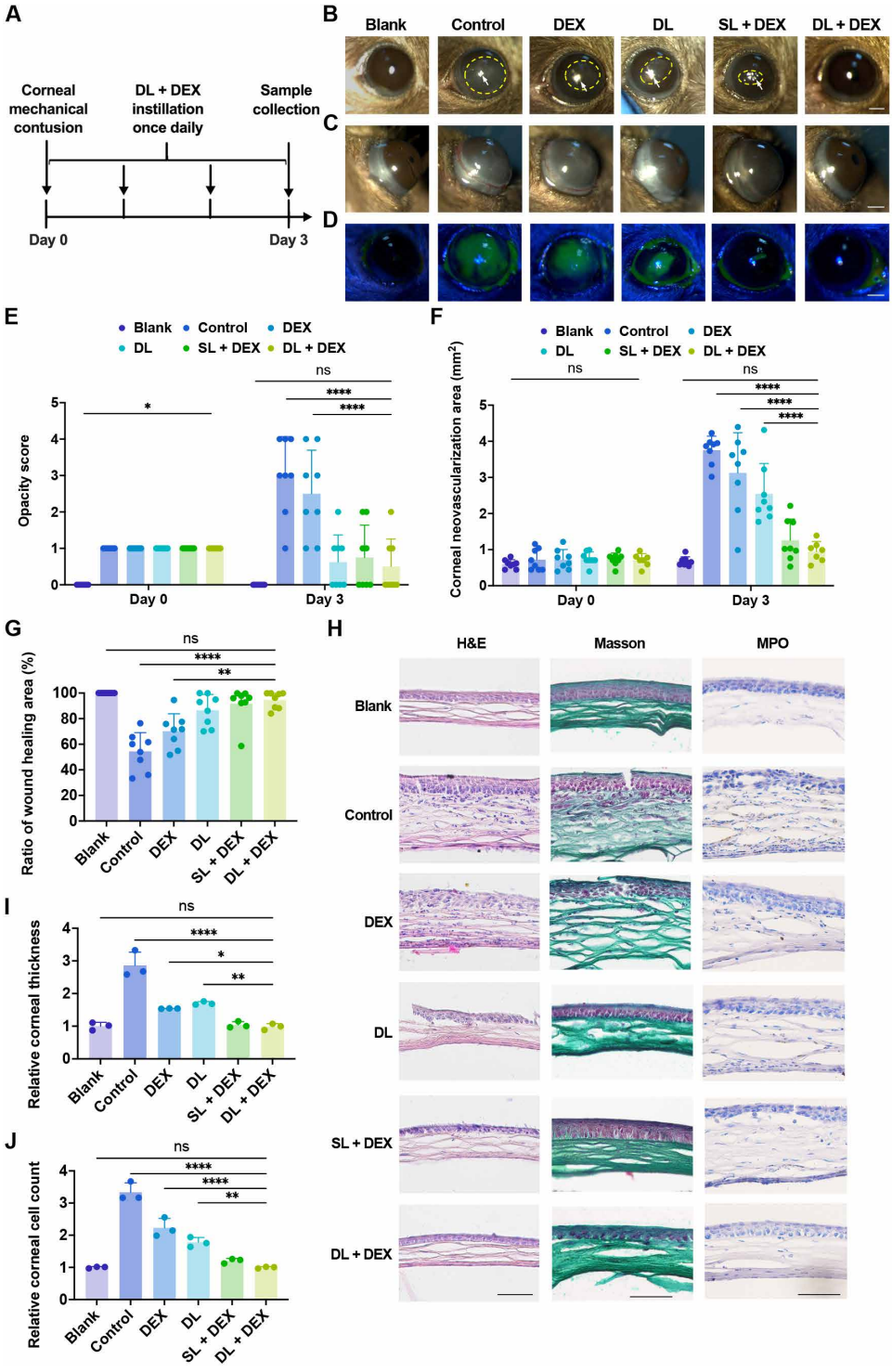

Fig. 5. Therapeutic effects of the drug-loaded nanocoating on mouse model of corneal contusion. (**A**) A flowchart of evaluating the treatment efficacy of the nanocoating in the corneal contusion mouse model. (**B**) Orthostatic images of mouse eyes under white light. Yellow dashed circle indicates corneal opacity region and white arrow points to uneven light reflection area. Scale bar, 1 μm. (**C**) Lateral images of mouse eyes under white light. Scale bar, 1 μm. (**D**) Images of mouse eyes under cobalt blue filter after fluorescein sodium staining. Scale bar, 1 μm. (**E**) Corneal opacity scores of the treated mice ($n = 8$). (**F**) Area of corneal neovascularization of the treated mice ($n = 7$ to 8). (**G**) Ratio of corneal wound healing area of the treated mice ($n = 8$). (**H**) Corneal sections showing H&E, Masson, and myeloperoxidase (MPO) staining (from left to right). Scale bars, 100 μm. (**I**) Relative corneal thickness of the treated mice ($n = 3$). (**J**) Relative cell counts in the mouse cornea ($n = 3$). Statistical analysis was performed using a one-way ANOVA with Tukey's multiple comparison test for multigrouped data and a two-way ANOVA followed by Tukey's post hoc test for multi–time-point longitudinal data, giving P values. *$P < 0.05$, **$P < 0.01$, and ****$P < 0.0001$. ns, no significance.

potential of ALJN. Chemical damage to ocular surface is a common ocular emergency, with an estimated incidence of 5.1 to 50 cases per 100,000 population per year (*45*). Ocular alkali burn account for 11.5 to 22.1% of all ocular injuries and are considered one of the most serious types of ocular chemical injuries (*46*). However, current available treatments of alkali burn suffer several limitations, such as frequent administration, low bioavailability, and unsatisfactory therapeutic effects. Correspondingly, as illustrated in Fig. 6A, we constructed a corneal alkali burn model by treating mice with sodium hydroxide (NaOH) according to methods reported elsewhere (*47*). The corneas of healthy mice were transparent, with no defects upon staining with sodium fluorescein. Differently, increased opacity was observed at the injury site in the modeled mice, which appeared white and large area of staining. Starting from the day of modeling, different groups of mice were received eye drop instillation of DEX, DL, SL + DEX, and DL + DEX once a day for five consecutive days, respectively. The control group (instillation with the same dose of PBS) and nonmodeled blank group were used for comparison to observe the therapeutic efficacy. During the course of treatment, we monitored the corneal opacity, area of corneal neovascularization, and area of corneal damage of the mice using a slit lamp (Fig. 6, B to D). On day 5 of treatment, a significant decrease in corneal opacity was observed in the DL + DEX group, where the pupils and irises could be visualized. While in the SL + DEX group, the pupils and irises were less visible. However, the DEX group and the control group showed negligible changes, with the pupils almost indistinguishable. After scoring the corneal opacity of each mouse (Fig. 6E), it was found that the DL + DEX group (2.29 ± 1.11 points) exhibited significantly superior improvement compared to the control group (3.86 ± 0.38 points) and the DEX group (3.57 ± 0.53 points), indicating that the combination of DL and DEX was effective in reducing corneal opacity. The DL + DEX group demonstrated a significantly improved inhibitory effect on corneal neovascularization compared to the DEX group and the control group (Fig. 6F). It was noted that the corneal neovascularization in the control group extended to half of the cornea (5.54 ± 0.77 mm^2). In the DEX group, it extended to about one-third (4.45 ± 0.56 mm^2), while in the DL + DEX group, the corneal neovascularization was hardly observed to extend (1.54 ± 0.67 mm^2). The degree of wound healing was assessed based on the ratio of the area of sodium fluorescein staining relative to the area on the day of modeling (Fig. 6G). The results clarified that the degree of wound healing in the DL + DEX group (76.32 ± 13.47%) was significantly higher than that in the control (31.25 ± 22.15%) and DEX groups (35.88 ± 15.00%). However, there was no significant difference between the DEX and control groups.

Besides the visible destruction of epithelial integrity observed under the slit lamp, corneal edema and infiltration of inflammatory cells and factors are also common histopathological manifestations of corneal injury (*48*). Accordingly, histological examination of mouse corneas was conducted after treatment using H&E and Masson staining (Fig. 6H). The corneal sections from the DL + DEX group exhibited well-arranged and clear corneal epithelial and stromal layers, similar to those from the blank group. However, in comparison, the corneas in the DEX and control groups displayed largely thickened stroma with edema, infiltration of inflammatory cells, and relatively disordered arrangement of epithelial cells. The DL + DEX group was found to have a notable difference in inhibiting corneal oedema and inflammatory cell infiltration compared to the DEX and control groups, indicating superior efficacy in these aspects (Fig. 6, I and J). Neutrophils and their lysates have been reported to slow down the healing of corneal epithelium in mice and can also secrete inflammatory factors that further damage the cornea (*49*). Therefore, we further conducted immunostaining on the corneal sections and found that DL + DEX was able to potently inhibit the infiltration of neutrophils and macrophages (Fig. 6H). The aforementioned results demonstrated that in the corneal alkali burn injury model with more severe inflammation, the therapeutic effect of DL was superior to that of SL drug-loaded nanocoating.

We further constructed a rabbit corneal alkali burn model to evaluate the therapeutic potential of ALJN in an animal model anatomically closer to the human eye. As illustrated in Fig. 7A, rabbit cornea was treated with 1 M NaOH for 30 s to induce corneal alkali burn injury and administered once daily for seven consecutive days. Corneal opacity, neovascularization area, and injury area were monitored throughout the treatment period (Fig. 7, B to D). On day 7, the DL + DEX group demonstrated a significant reduction in corneal opacity, with the pupil and iris clearly visible, whereas the DEX and control groups displayed no distinguishable pupil features. Corneal opacity scores showed that the DL + DEX group (2.40 ± 0.54 points) significantly outperformed both the control group (3.50 ± 0.57 points) and the DEX group (3.50 ± 0.57 points) (Fig. 7E), indicating that the combined use of DL and DEX was effective in decreasing corneal opacity. The DL + DEX group also exhibited superior inhibition of corneal neovascularization (Fig. 7F), with a neovascularized area of 33.92 ± 8.41 mm^2, markedly smaller than the DEX group (68.42 ± 9.98 mm^2) and control group (112.49 ± 15.22 mm^2). Wound healing, evaluated by the ratio of sodium fluorescein–stained area to the initial injury area (Fig. 7G), was significantly enhanced in the DL + DEX group (97.34 ± 1.74%) compared to the control group (62.09 ± 7.52%) and the DEX group (83.30 ± 2.68%). Histological analysis of the treated rabbit corneas was also performed (Fig. 7H). H&E and Masson staining revealed that the corneal sections in the DL + DEX group closely resembled those in the blank group, with orderly arranged corneal epithelium and stroma. In contrast, the DEX group showed notable stromal thickening, edema, inflammatory cell infiltration, and disordered epithelial cell arrangement compared to the blank group, with statistically significant differences in relative corneal thickness (Fig. 7I). Immunostaining of corneal sections further demonstrated that DL + DEX effectively inhibited the distributions of TNF-α and macrophages in the injured cornea, similar to the mouse model. In addition, relative concentrations of TNF-α and IL-6 in the cornea were measured (Fig. 7, J and K), confirming significant suppression of inflammatory factors by DL + DEX compared to DEX. Collectively, these findings indicated that in rabbit corneal alkali burn models, the DL drug-loaded nanocoating exhibited superior therapeutic efficacy compared to SL, highlighting the potential of ALJN for managing corneal alkali burn injury.

DISCUSSION

In this study, we introduce a type of eye drops basing on a Janus nanocoating structure with different properties on two sides, capable of forming a durable drug-loaded nanocoating on ocular surface while maintaining satisfactory comfort and preventing eyelid adhesion. This well-structured bilayer nanocoating is simply formed through complexation interactions between polyphenolic compound TA and metal ion Fe^{3+} as well as the phosphorylcholine pendent groups of PMPC and metal ion Fe^{3+}. Following sequential topical

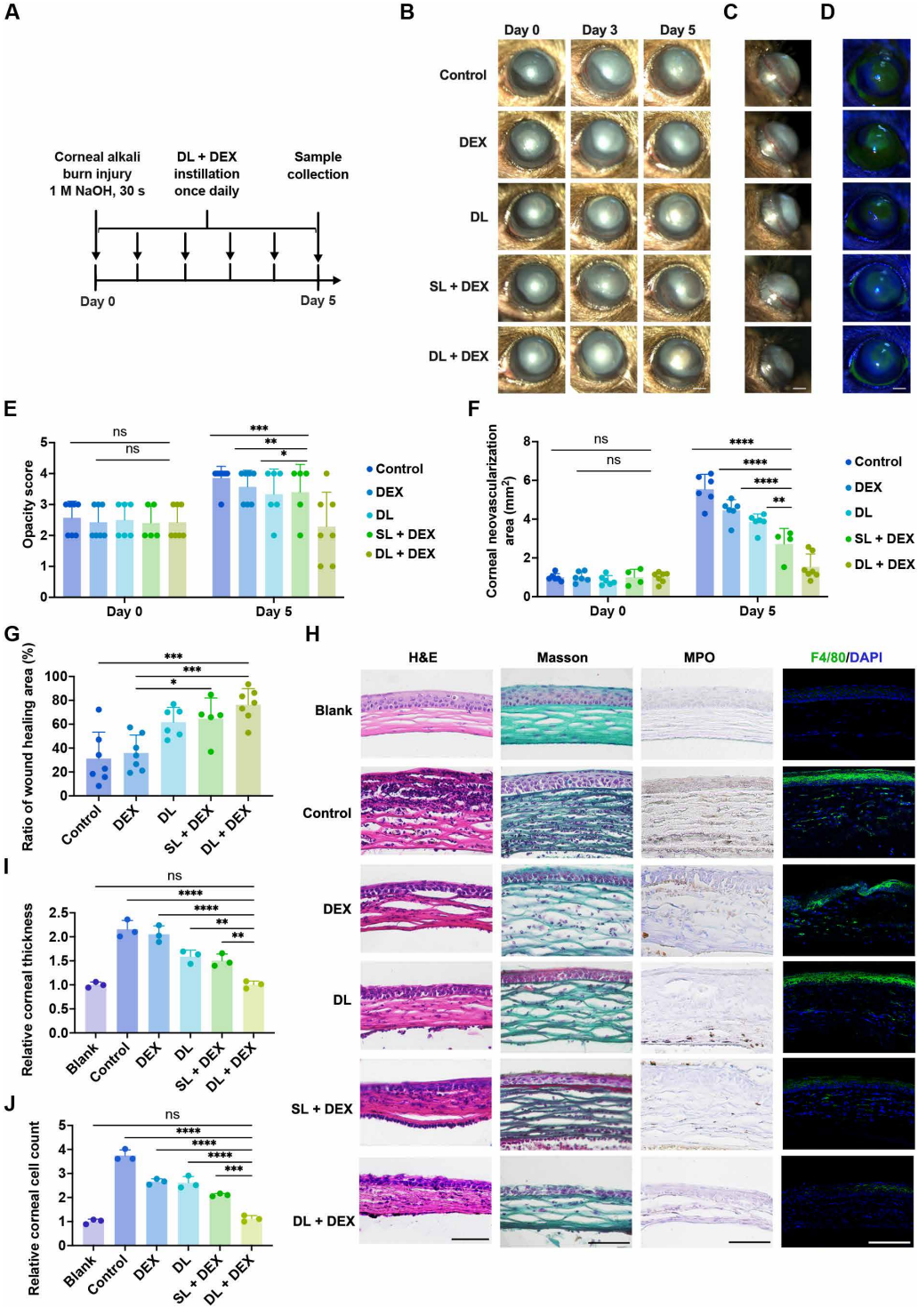

Fig. 6. Therapeutic effects of the drug-loaded nanocoating on mouse models of corneal alkali burn. (**A**) A flowchart of evaluating the treatment efficacy of the nanocoating in the corneal alkali burn mouse model. (**B**) Orthostatic images of mouse eyes under white light. Scale bar, 1 μm. (**C**) Lateral images of mouse eyes under white light. Scale bar, 1 μm. (**D**) Images of mouse eyes under cobalt blue filter after fluorescein sodium staining. Scale bar, 1 μm. (**E**) Corneal opacity scores of the treated mice ($n = 5$ to 7). (**F**) Area of corneal neovascularization of the treated mice ($n = 4$ to 7). (**G**) Ratio of corneal wound healing area of the treated mice ($n = 5$ to 7). (**H**) Corneal sections showing H&E, Masson, and MPO staining, as well as F4/80 immunofluorescence staining (from left to right). Scale bars, 100 μm. (**I**) Relative corneal thickness of the mice after different treatments ($n = 3$). (**J**) Relative cell counts in the mouse cornea ($n = 3$). Statistical analysis was performed using a one-way ANOVA with Tukey's multiple comparison test for multigrouped data and a two-way ANOVA followed by Tukey's post hoc test for multi–time-point longitudinal data, giving P values. $^{*}P < 0.05$, $^{**}P < 0.01$, $^{***}P < 0.001$, and $^{****}P < 0.0001$. ns, no significance.

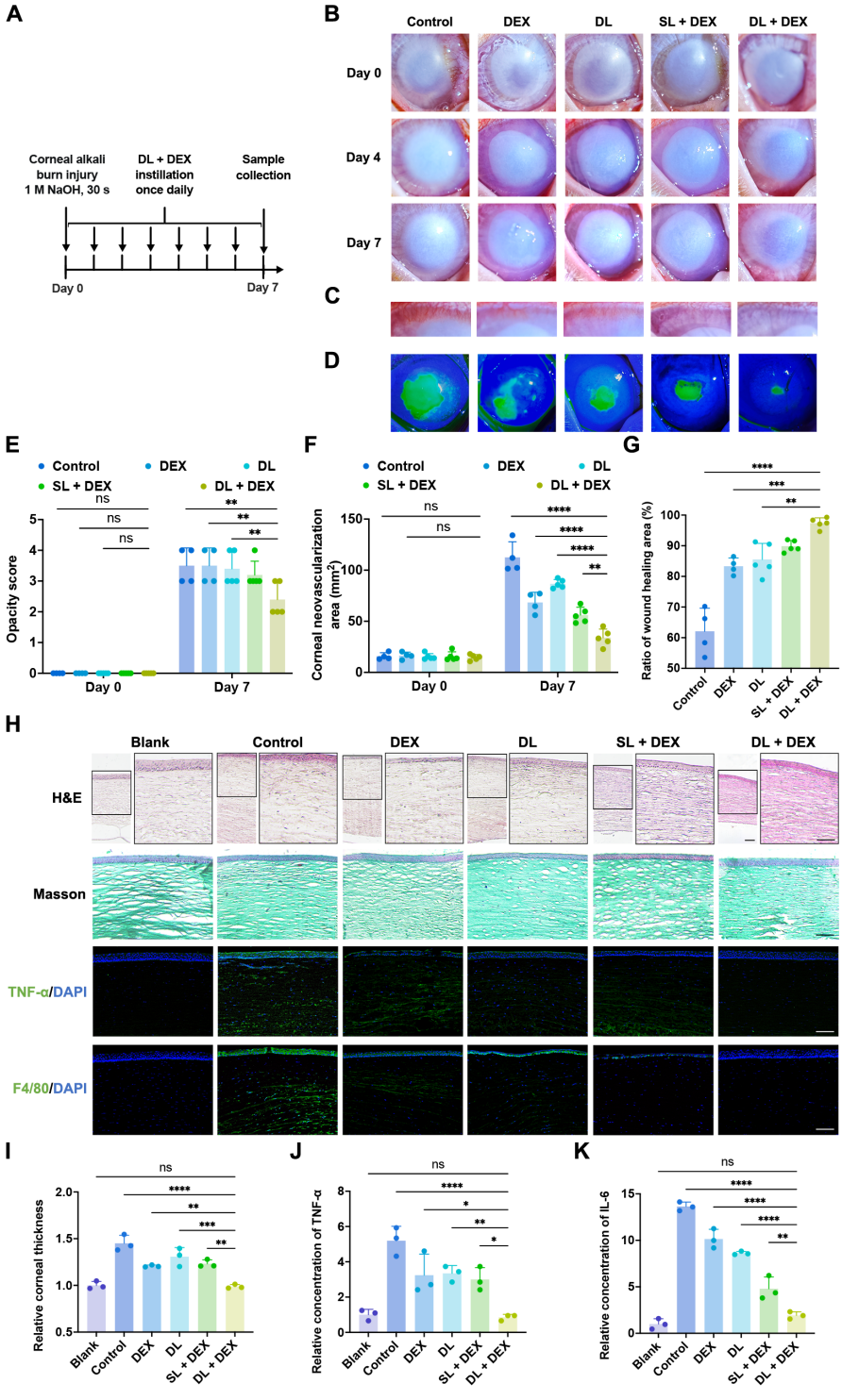

Fig. 7. Therapeutic effects of drug-loaded nanocoating on rabbit models of corneal alkali burn. (**A**) A flowchart of evaluating the treatment efficacy of the nanocoating in the corneal alkali burn rabbit model. (**B**) Orthostatic images of rabbit eyes under white light. (**C**) Lateral images of rabbit eyes under white light. (**D**) Images of rabbit eyes under cobalt blue filter after fluorescein sodium staining. (**E**) Corneal opacity scores of the treated rabbits ($n = 4$ to 5). (**F**) Area of corneal neovascularization of the treated rabbits ($n = 4$ to 5). (**G**) Ratio of corneal wound healing area of the treated rabbits ($n = 4$ to 5). (**H**) Corneal sections showing H&E and Masson staining, as well as TNF-α and F4/80 immunofluorescence staining (from top to bottom). Scale bars, 100 μm. (**I**) Relative corneal thickness of the rabbits after different treatments ($n = 3$). Relative concentrations of (**J**) TNF-α and (**K**) IL-6 in the corneas of rabbits under different treatments ($n = 3$). Statistical analysis was performed using a one-way ANOVA with Tukey's multiple comparison test for multigrouped data and a two-way ANOVA followed by Tukey's post hoc test for multi–time-point longitudinal data, giving *P* values. $^{*}P < 0.05$, $^{**}P < 0.01$, $^{***}P < 0.001$, and $^{****}P < 0.0001$. ns, no significance.

administration in the form of eye drops, two layers are spontaneously assembled on ocular surface to form a bilayer nanocoating structure. The formed inner layer generates a reservoir for drug loading and controlled release due largely to its network structure and adhesive feature. The drug-loaded adherent inner layer can sustainedly retain on ocular surface for a prolonged period, providing a sustained release of drug. In addition to its drug loading and adhesive properties, the component of TA has a natural anti-inflammatory ability. The lubricating outer layer offers an interfacial lubricating capability, ensuring comfort and preventing the adhesion between the nanocoating and eyelid. Meanwhile, the nanocoating exhibits favorable biocompatibility, without causing tissue damage or other adverse effects.

The nanocoating demonstrates prolonged residence duration on ocular surface both in vitro and in vivo. Free form drugs exhibit almost no detectable retention on corneal surface after just 2 hours post-instillation, while the nanocoating shows extended residence for up to 24 hours. The encapsulated DEX in the nanocoating also verifies a sustained release profile for over 24 hours, indicating its ability to provide a basis for the intervention of dosing frequency. This implies that a once-daily instillation may enable an adequate topical concentration of dosed drugs on ocular surface, playing an enhanced therapeutic efficacy. The reduction in dosing frequency implies an improvement in compliance, which is beneficial for treatment (*50*). Compared to other ocular drug delivery systems, this nanocoating eye drops have the advantages of both adhesive and lubricating. The blink times within 5 min after instillation on mouse ocular surface are significantly lower than that of the adhesive coating and similar to normal mice, suggesting satisfied ocular surface comfort. The improvement in comfort can tremendously enhance compliance, which is critical for developing eye drops (*51*). Briefly, this type of nanocoating eye drops is able to reduce dosing frequency through prolonging adhesion and sustaining drug release and ensure ocular surface comfort via introducing a lubricating interface.

Corneal injury is an acute ocular surface disease that requires prompt treatment (*52*). After corneal injury, cells in all layers of the cornea engage in cell proliferation, migration, extracellular matrix remodeling, and secretion and aggregation of chemokines, growth factors, cytokines, etc., resulting in an inflammatory response (*52*). The involvement of corneal stromal cells also triggers apoptosis and the transform of corneal cells to fibroblasts, causing in a decrease in crystallins and an increase in corneal opacity (*53*). During this pathological process, the balance between angiogenic and inhibitory factors is altered, and the vascular barrier of the corneal limbus is disrupted, promoting the formation of corneal neovascularization (*54*). This is a major pathological change leading to visual impairment and even blindness (*55*). After corneal injury, varying degrees of decreased transparency, neovascularization, and inflammatory responses are exhibited, with severe cases potentially leading to blindness (*56*). Therefore, these need to be rescued in time. However, the presence of the ocular surface barrier causes low bioavailability of drugs. Our results indicate that treatment with nanocoating in mice and rabbits with corneal contusion and alkali burn achieves a significant decrease in corneal opacity, a reduction in the degree of neovascularization, and a higher proportion of wound healing area compared to the drug-only intervention group. In addition to clinical manifestations, histopathological examinations are conducted on treated animals. Treatment with the nanocoating shows corneal thickness and structural arrangement closer to that of normal animals, with less corneal edema and lower levels of inflammatory cell infiltration. Meantime, inflammatory factors in the corneal tissue—such as TNF-α, IL-6, and IL-1β—are also closer to normal levels. Collectively, our nanocoating can effectively improve the corneal transparency of mice and rabbits, inhibit corneal neovascularization, accelerate the repair of corneal injuries, and suppress the infiltration of inflammatory cells and factors.

In summary, this study reports a Janus nanocoating ocular drug delivery system that has the capabilities of prolonging ocular surface residence, sustaining drug release, providing ocular surface comfort, and performing a dual anti-inflammatory function, demonstrating its potential for the treatment of corneal injuries. For future perspective, the safety of this nanocoating needs to be investigated systemically, and the therapeutic values toward other disease models are worth studying. Moreover, future work on the exploration of the application of this nanocoating to carry other drugs and on the optimization of the most appropriate dosage and frequency of administration, particularly in advanced animal models, is anticipated. Overall, the drug-loaded Janus nanocoating holds promise as a simple yet effective approach for treating ocular diseases.

MATERIALS AND METHODS

Reagents

The chemicals used in this study included TA (Aladdin, Shanghai, China), iron (III) chloride hexahydrate (Fe^{3+}) (BBI, Shanghai, China), 2-methylpropylene glycol phosphate choline (MPC) (Bidepharm, Shanghai, China), azobisisobutyronitrile (AIBN) (Rhawn, Shanghai, China), FITC (Aladdin), and NaOH (BBI). The water used in the experiment underwent purification through the Millipore Milli-Q purification system.

Animals

The male C57BL/6J mice (6 to 8 weeks old) were purchased from SiPeiFu (Beijing) Biotechnology Co. Ltd. Mice were randomly grouped. Mice were housed and fed in specific pathogen–free environments under a controlled condition of 12-hour light/12-hour dark cycles at 20° to 22°C. New Zealand white rabbits (1.5 to 2.5 kg) were provided by Shanghai Chedun Experimental Animal Co. Ltd and randomly grouped. All animal experiments were carried out according to the institutional guidelines and approved by Animal Care and Use Committee in Shanghai Yishang Biotechnology company (IACUC-2024-Mi-054).

Synthesis of PMPC

The MPC monomer and AIBN initiator were combined in a reaction flask and subjected to vacuum drying to remove moisture. Following this, the mixture was dissolved in methanol. To eliminate oxygen from the system, the reaction mixture was purged with nitrogen gas for 30 min. Subsequently, the flask was heated in a water bath to 60°C and react for 10 hours. After the reaction, the mixture was cooled in an ice bath. The reaction mixture was then precipitated in a large amount of ice-cold diethyl ether, to get white, gelatinous precipitate. This precipitate was collected by centrifugation and washed three times to remove impurities. The final product, PMPC, was obtained through freeze drying.

Characterization of the nanocoating

The ^{1}H NMR spectroscopy (Bruker Avance Neo 400 M, Billerica, MA, USA) and FTIR spectroscopy (Thermo Scientific Nicolet iS50,

Waltham, MA, USA) were used to measure the obtained PMPC. The sample was sonicated for 5 min before the ^{1}H NMR measurement. ^{1}H NMR of MPC (400 MHz, deuterated water): 6.05 (d, J = 0.9 Hz, 1H), 5.67 to 5.56 (m, 1H), 4.34 to 4.21 (m, 2H), 4.15 (qd, J = 7.3, 2.6 Hz, 2H), 4.02 (ddd, J = 6.7, 4.5, 2.8 Hz, 2H), 3.52 (dd, J = 5.8, 3.2 Hz, 2H), 3.08 (d, J = 5.5 Hz, 9H), and 1.86 to 1.74 (m, 3H). ^{1}H NMR of PMPC (400 MHz, deuterated water): 4.17 (d, J = 17.1 Hz, 2H), 4.12 (s, 1H), 3.98 (s, 2H), 3.58 (s, 2H), 3.11 (d, J = 17.7 Hz, 9H), 2.02 to 1.66 (m, 1H), 0.98 (s, 1H), and 0.82 (s, 1H) (fig. S1). In the FTIR spectrum of PMPC (fig. S2), the peak at 1238 cm^{-1} corresponded to the stretching vibration absorption of the P═O bond, and the peak at 1076 cm^{-1} was attributed to the stretching vibration absorption of the P—O—C bond. In addition, the disappearance of the C═C stretching vibration peak at 1635 cm^{-1}, originally presented in MPC monomer, further confirmed the successful preparation of PMPC.

The surface morphology of SL and DL was photographed using SEM (Hitachi, Regulus 8230, Tokyo, Japan) and TEM (Hitachi, HT7700). Silicon wafers were immersed in piranha solution for 10 min, followed by ultrasonic cleaning in deionized water for 10 min, rinsed with ethanol, and blown dry with nitrogen gas. SL and DL were dropped onto clean silicon wafers separately and dried before SEM imaging. SL and DL were applied to 400-mesh carbon grids and left to settle for 10 min. Excess liquid was absorbed away with filter paper, and the grids were air-dried before imaging with TEM.

The surface roughness of the nanocoating was measured using AFM (Bruker NanoWizard, Billerica, MA, USA). The SCANASYST-AIR probe was used for imaging the cornea and the nanocoating. All imaging experiments were conducted in a vibration-isolation enclosure at room temperature. For each sample, the indentation force curves were generated with a force set point of 5 nN using the "PeakForce quantitative imaging" operating mode.

The thickness of the nanocoating was measured using SEM and a step profiler (KLA, Alpha-step D-600, Milpitas, CA, USA). Agar slices and cornea were dropped with SL and DL, respectively. After freeze-drying, the samples were fractured in liquid nitrogen and then observed under SEM for cross-sectional examination. Silicon wafers, prepared as described in the previous steps, were dropped with SL and DL solutions for 1 min, separately. After being gently rinsed twice with deionized water and air-dried, the thickness was quantified using the step profiler.

The interaction between Fe^{3+} ions and PMPC was characterized using an ultraviolet spectrophotometer (Agilent 8454, Santa Clara, CA, USA). Solutions of Fe^{3+} ions (0.8 mg/ml), alone or mixed with PMPC (1 mg/ml) in equal volumes, were vortexed for 30 s, and their spectral scans were performed using the spectrophotometer.

The presence of DEX in the nanocoating was characterized using a mass spectrometer (Thermo ISQ EM, Waltham, MA, USA) and a FTIR spectroscopy. A 0.3% (w/v) agar gel was prepared. A volume of 200 μl of Fe^{3+} (0.8 mg/ml) solution was added to a 48-well plate lined with agar gel and vortexed for 1 min. Then, 200 μl of TA (5 mg/ml) solution was added and vortexed for another min, followed by the addition of 100 μl of DEX (10 mg/ml), vortexed for 5 min. The supernatant was then discarded, and the gel was washed twice with deionized water. A spatula soaked in the solution was used to extract the gel, and approximately a 5-mm section containing the surface coating was cut out, placed in 2 ml of deionized water, and vortexed for 30 min to dissolve. The sample was then filtered through a 0.22-μm filter membrane and analyzed using a mass spectrometer. A 1% (w/v) agar gel was used as a substrate in a 48-well plate. Fe^{3+} (0.8 mg/ml) and TA (5 mg/ml) were sequentially added onto the agar surface in equal volumes, followed by an incubation period of 1 min. Subsequently, a solution of DEX (10 mg/ml) was introduced and incubated for 5 min. Thereafter, a solution of PMPC (1 mg/ml) was added onto the agar gel surface and incubated for an additional min. The entire solution was then aspirated, and the gel was rinsed twice. A 5-mm section of the gel containing the nanocoating was cut out and incubated in water for 4 hours to soften the agar gel. The drug-loaded agar gel, along with the solution, was subjected to freeze-drying. The resulting solid was then characterized by FTIR.

The surface wettability of the nanocoating was characterized using a contact angle tester (Krüss, Hamburg, Germany). Silicon wafers were immersed in SL and DL solutions for 1 min. The excess fluid was then blotted away with filter paper. After air-drying for 5 min, the static contact angle of the nanocoating was measured using the sitting drop method.

Drug loading and in vitro drug release

Using a previously established standard curve for DEX, the loading amount of DEX and its release profile were examined using HPLC (Agilent 1260 Infinity II). The ocular surface environment was simulated with 1% agar, onto which Fe^{3+} (0.8 mg/ml) and TA (5 mg/ml) were added and mixed with DEX to form the SL layer. After mixing, the supernatant was discarded, and PMPC (1 mg/ml) was added to form the DL structure. Once the nanocoating had stabilized, the supernatant was taken, and the unencapsulated DEX was quantified using HPLC in triplicate samples. The efficiency of DEX encapsulation was calculated on the basis of these measurements. Similarly, after the nanocoating had stabilized, the supernatant was replaced with PBS and continuously shaking on the vortexer. At various time points (5, 10, 15, 30, and 45 min, as well as 1, 1.5, 2, 2.5, 3, 4, 5, 6, 7, 8, 9, 10, 11, 12, and 24 hours), aliquots of the supernatant were taken, and the concentration of released DEX at each time point was quantified using HPLC to calculate the percentage of drug release. The HPLC conditions were as follows: a diamonsil C18 chromatographic column (5 μm, 150 mm by 4.6 mm) was used. The mobile phase consisted of a 30:70 mixture of acetonitrile and water. The column temperature was maintained at 37°C, and the absorbance wavelength was set at 240 nm. The injection volume was 5 μl, and the flow rate was 1.0 ml/min.

In vitro biocompatibility of the nanocoating

The biocompatibility of the coating was assessed using the CCK-8 assay (Beyotime, Shanghai, China) in epithelial cells. Cells were seeded at a density of 10,000 cells per well in a 96-well plate and exposed to different components of the nanocoating, with six replicates per group. Subsequently, the plates were incubated under conditions of 37°C, 90% humidity, and 5% CO_2 for 24 hours. After the incubation period, the supernatant was removed, and the cells were washed twice with 100 μl of PBS. Then, 100 μl of culture medium containing 10 μl of CCK-8 solution was added to each well, and the plates were returned to the incubator under the aforementioned conditions for an additional hour. The optical density at 450 nm was measured using a multifunction microplate tester (BioTek, Vermont, USA), and from this, the cell viability was calculated.

In vitro anti-inflammatory effects of the nanocoating

The in vitro anti-inflammatory function of the nanocoating was evaluated by measuring NO production using a NO assay kit (Beyotime).

J774A.1 cells, a mouse macrophage cell line commonly used to study inflammatory responses, were seeded at a density of 10,000 cells per well in a 96-well plate. The cells were then co-incubated with different components of the nanocoating, with three replicates per group. After that, 100 μl of complete culture medium containing of LPS (100 μg/ml; Beyotime, China) was added to each well to stimulate the cells. The plate was then incubated for 24 hours under the same conditions as mentioned previously. After the incubation, the NO detection reagents were used. To each well, 50 μl of Griess reagent I was added, followed by 50 μl of Griess reagent II. After allowing the reaction to proceed for a short period, the optical density at 450 nm was measured using a multifunction microplate tester. The measured absorbance was then compared to the previously examined NO standard curve to calculate the concentration of NO produced in each sample.

The in vitro anti-inflammatory properties of the nanocoating were investigated by analyzing macrophage polarization and quantifying the secreted inflammatory factors. RAW264.7 cells were seeded at a density of 1×10^6 cells per well in a six-well plate and cultured in 2 ml of complete growth medium for 24 hours. After refreshing the medium, the cells were co-incubated with various nanocoating components and stimulated with LPS (1 μg/ml) for an additional 24 hours, with three replicates per group. The conditioned medium was then collected, and the concentrations of IL-6 and TNF-α were measured using enzyme-linked immunosorbent assay (ELISA) kits (Multi Sciences, Hangzhou, China). Macrophage polarization was evaluated by flow cytometric analysis of specific surface markers. Cells were gently detached using 1 ml of PBS, resuspended in centrifuge tubes, and centrifuged at 400*g* for 5 min at 4°C. The supernatant was discarded, and the cells were resuspended in 200 μl of PBS in a 96-well U-bottom plate and precipitated by centrifugation. After discarding the supernatant, 10 μl of purified anti-mouse CD16/32 antibody (1:500; BioLegend, San Diego, CA, USA) diluted in PBS was added and incubated at room temperature for 15 min. Subsequently, a mixture of PE anti-mouse CD80 antibody (1:500; BioLegend) and allophycocyanin anti-mouse CD86 antibody (1:500; BioLegend) diluted in PBS (40 μl) was added and incubated on ice for 30 min. The samples were washed twice with 200 μl of PBS, fixed with 50 μl of a fourfold-diluted Fixation/Permeabilization Concentrate (Invitrogen, Carlsbad, CA, USA), and incubated at room temperature for 30 min. After centrifugation, cells were permeabilized using 1× Permeabilization Buffer (Invitrogen) and stained with FITC anti-mouse CD206 antibody (1:500; BioLegend) in the dark on ice for 30 min. The samples were washed thrice, resuspended in PBS, and analyzed using flow cytometry (BD biosciences FACSVerse, NJ, USA).

In vitro retention duration of the nanocoating

On the surface of 1% agar, Fe^{3+} ions (0.8 mg/ml) and TA (5 mg/ml) were added and mixed with sodium fluorescein (0.1%) (Adamas, Shanghai, China). After thorough mixing, the supernatant was discarded, and PMPC (1 mg/ml) was then added to form the DL structure. For the control group, all components except sodium fluorescein were replaced with PBS. Once the coating had stabilized, the supernatant was discarded, and PBS was added. Different groups of coated agar surface were then shaking on a vortexer during different periods of time: 0, 1, 2, 4, 8, and 24 hours. The coating was illuminated using cobalt blue light, and photographs of the nanocoating were taken to measure the average fluorescence intensity of the green fluorescence. This intensity was compared to the intensity at the 0-hour time point to calculate the proportion of residual fluorescence.

In vivo retention time of the nanocoating on ocular surface

The synthesis of TA-FITC: TA was stirred with 25 to 28% $NH_3 \cdot H_2O$ for 1 hour. The mixture was then dried at 80°C. The product was subsequently added to a 0.1 M Na_2CO_3 buffer solution at pH 9.0, and a dimethyl sulfoxide solution of FITC was introduced. The reaction was allowed to proceed overnight, and the product was then dialyzed to obtain a solution of TA-FITC. For the control group, a suspension of FITC was prepared and its fluorescence intensity was measured at various concentrations using a fluorescence spectrophotometer (Horiba, Kyoto, Japan). The concentration of FITC that exhibited the same fluorescence intensity as the TA-FITC suspension (5 mg/ml) was examined to be 4.3 μg/ml.

Male C57BL/6J mice (6 to 8 weeks old) were used. A mixture containing Fe^{3+} (0.8 mg/ml) and TA-FITC (5 mg/ml), in equal volumes, was prepared and 20 μl of which was administered to ocular surface of unanesthetized mice, respectively. The eye drops were applied, and the mice were observed for 30-s post-administration, after which the blinking of the eyes was not hindered. For the control group, the solution was replaced with PBS solution of FITC. The mice were euthanized at different time points after ocular administration: 0.5, 2, 4, 8, and 24 hours. The eyes were fixed with eye ball fixed liquid (Servicebio, Wuhan, China) and then embedded in Tissue-Tek O.C.T. (Sakaru Finetek, Tokyo, Japan) for frozen sectioning. The cell nuclei were stained with 4′,6-diamidino-2-phenylindole (DAPI) (Beyotime), a fluorescent dye that binds to DNA. Laser scanning confocal microscopy (LSCM) (Leica, Nussloch, Germany) was used to capture the images of the cornea.

In vivo drug release of the nanocoating

New Zealand white rabbits (1.5 to 2.5 kg) were anesthetized with Zoletil 50 (15 mg/kg; Virbac, Carros, France), followed by rinsing their eyes with PBS. Then, 20 μl of ALJN containing DEX (1 mg/ml) was instilled onto ocular surface. Tear samples were collected at 0.5, 2, 4, 6, and 24 hours post-administration by immersing a 0.5 cm–by–1 cm long square filter paper into the lower conjunctival sac for 30 s. The DEX content in the tear fluid was detected using HPLC, and the drug release ratio at each time point was calculated.

Animal models of corneal contusion and corneal alkali burn

The corneal contusion mouse model was also established using a previously published method (*57*). Male C57BL/6 J mice, aged 6 to 8 weeks, were anesthetized with isoflurane (RWD, Shenzhen, China) for approximately 5 min. The ocular surface was topically anesthetized with 0.4% benoxinate hydrochloride. Excess liquid in the conjunctival sac was wiped away. Whiskers and eyelashes were trimmed with scissors to facilitate full eyelid opening. A 2-mm circular corneal trephine was used to mark the area of intervention, followed by mechanical injury to the corneal surface using scissors, and an epithelial scraper to create the contusion. Last, the cornea was flushed with PBS for 1 min.

The corneal alkali burn mouse model was established using a previously published method. Male C57BL/6J mice, aged 6 to 8 weeks, were anesthetized with isoflurane for approximately 5 min. The ocular surface was topically anesthetized with 0.4% benoxinate hydrochloride (Aladdin). Excess liquid in the conjunctival sac was wiped away. A single-layer circular filter paper with a diameter of 2 mm was soaked in a 1 M NaOH solution for 30 s and then placed on a piece of dry filter paper for 1 s to remove excess alkali liquid. After that, the filter paper was placed on the central cornea of the mouse, gently

pressed, and left for 30 s before being removed. The cornea was then flushed with saline for 1 min.

The corneal alkali burn rabbit model was established following a previously published method (*58*). New Zealand white rabbits (1.5 to 2.5 kg) were anesthetized with Zoletil 50 (15 mg/kg) for approximately 15 min. The ocular surface was topically anesthetized with 0.4% benoxinate hydrochloride (Aladdin), and the excess fluid in the conjunctival sac was carefully removed. An 8-mm-diameter single-layer circular filter paper, soaked in a 1 M NaOH solution for 30 s, was lightly blotted on a dry filter paper for 1 s to remove excess alkali solution and subsequently placed on the central cornea. The filter paper was gently pressed and left for 30 s before being removed. Last, the cornea was flushed with saline for 1 min.

In vivo therapeutic efficacy of the nanocoating

To evaluate the therapeutic effects of different components of the nanocoating, the following experimental groups were established, with each group receiving topical instillation once daily: (i) healthy animals treated with PBS serving as the blank control group (blank), (ii) model animals treated with PBS serving as the control group (control), (iii) model animals treated with a DEX solution (DEX), (iv) model animals treated with DL without drug (DL), (v) model animals treated with SL with DEX (SL + DEX), and (vi) model animals treated with DL with DEX (DL + DEX).

Before the preparation of the nanocoating, all components were filtered through a 0.22-μm filter to ensure sterility. Subsequent operations were carried out in a sterile environment to prevent contamination, maintained until administration. The SL layer was prepared by mixing equal volumes of Fe^{3+} (0.8 mg/ml) and TA (5 mg/ml), and 10 μl of the solution was applied to the ocular surface of mice. For the DL treatment, an additional 10 μl of PMPC (1 mg/ml) was applied 30 s after the SL instillation, allowing for adequate interaction between the components. For the groups containing DEX, the final concentration of DEX was 1 mg/ml. In cases where a specific component was not included in a treatment group, an equal volume of PBS was used as a substitute to maintain consistency in treatment volume. Mice were not anesthetized during drug administration, while rabbits were anesthetized with Zoletil 50 (15 mg/kg) before drug administration.

Clinical assessment

Corneal opacity was assessed by two experts who scored the anterior segment images of the mouse corneas captured through a slit lamp. A scoring system of 0 to 4 was used for the results (0 = completely clear, 1 = slightly hazy with easy visibility of the iris and pupil, 2 = moderately cloudy with the iris and pupil still visible, 3 = opaque with the pupil almost invisible, and 4 = completely opaque and the pupil not visible at all) (*54*).

The area of corneal neovascularization was quantified by measuring the length of the neovascularization in the side view images of the mouse corneas taken with a slit lamp. The average length was used to calculate the area of neovascularization.

The area of corneal injury was measured through corneal fluorescein sodium staining. A volume of 1 μl of 0.1% fluorescein sodium was dropped into the conjunctival sac, and after 60 s, excess liquid was wiped away. The anterior segment images of the cornea were captured under the cobalt blue light filter of the slit lamp microscope. The area of corneal injury was determined by measuring the green fluorescent area of the cornea each day and by comparing it with the area on the day of injury to obtain the proportion of injury healing.

Histological and morphometric evaluation

After euthanizing the mice and rabbits, the eyeballs were removed and fixed using eye ball fixed liquid. The fixed eyeballs were then processed for paraffin embedding and sectioning. H&E staining was used to observe the morphology of corneal epithelial cells and the degree of stromal edema. The paraffin-embedded sections were deparaffinized and rehydrated before being immersed in hematoxylin solution for 5 min. After washing, the sections were immersed in acid alcohol differentiation solution for 30 s. Following another wash, the sections were briefly immersed in blueing buffer for 30 s. The sections were then washed, stained with eosin for 5 min, and washed again before undergoing a series of dehydration and clearing steps. Last, the sections were mounted and dried before observation. Masson's trichrome staining was used to observe the morphology of the corneal stroma and collagen deposition. After deparaffinization and rehydration, the sections were stained with hematoxylin solution for 5 min and then washed. Then, sections were incubated with acidic differentiation solution for 30 s, followed by rinsing with tap water to remove excess stain. The sections were then incubated with fuchsin-acidic magenta staining solution for 10 min, after which the excess stain was discarded. The sections were differentiated with phosphomolybdic acid solution for 1 min, followed by a brief incubation with light green staining solution for 30 s, and another differentiation step with acidic differentiation solution for 1 min. Last, the sections were dehydrated, cleared, and mounted. Images were captured using a phase contrast upright microscope (Nikon, Japan).

Immunohistochemical staining

After the mice and rabbits were euthanized, the eyeballs were removed and fixed using eye ball fixed liquid. The fixed eyeballs were then processed for paraffin embedding, and sections were prepared. The sections were deparaffinized and rehydrated, followed by antigen retrieval through boiling in antigen retrieval solution (Beyotime) for 1 hour. Once cooling to room temperature, the sections were blocked with 5% goat serum (Beyotime) for 1 hour to minimize nonspecific binding. After that, the sections were drained and incubated with the primary antibody [myeloperoxidase, rabbit polyclonal antibody (pAb), 1:1000, ABclonal, Wuhan, China] at 4°C overnight. The following day, the sections were washed and then incubated with the secondary antibody [1:300; horseradish peroxidase–conjugated goat anti-rabbit immunoglobulin G (IgG), Servicebio] at room temperature for 1 hour. After another round of washing, the sections were incubated with 3,3′-diaminobenzidine (DAB) color development kit (Beyotime) to visualize the bound antibodies for 5 min before being rinsed to stop the reaction. The cell nuclei were then stained with hematoxylin, and after further washing, the sections were dehydrated, cleared, and mounted. Images were captured using a phase contrast upright microscope.

Immunofluorescent staining

After the mice and rabbits were euthanized, the eyeballs were removed and fixed using eye ball fixed liquid. The fixed eyeballs were then processed for paraffin embedding, and sections were prepared. The sections were deparaffinized and rehydrated, followed by antigen retrieval through boiling in antigen retrieval solution for 1 hour. Once cooling to room temperature, the sections were blocked with

5% goat serum for 1 hour to minimize nonspecific binding. After that, the sections were drained and incubated with the primary antibody (1:1000; Rb pAb to TNF-α, Abcam, Cambridge, England; 1:200; F4/80 rabbit pAb, ABclonal, Wuhan, China) at 4°C overnight. At following day, the sections were washed and then incubated with the secondary antibody (1:200; Goat Anti-Rabbit IgG Alexa Fluor 488, Abcam) at room temperature for 1 hour away from light. Then, the cell nuclei were stained with DAPI before the sections were mounted. Images were captured using a LSCM.

Concentrations of inflammatory factors

After the mice and rabbits were euthanized, the eyeballs were removed, and the corneas were carefully separated from the rest of the ocular tissue. The isolated corneas were then used to extract protein using radio-immunoprecipitation assay lysis buffer (Beyotime). The protein concentration in each cornea sample was quantified and balanced using a bicinchoninic acid protein assay kit (Beyotime). After that, the levels of different inflammatory cytokines in the corneas were assessed using ELISA kits (Multi Sciences) specific for TNF-α, IL-1β, and IL-6. Then, the relative concentrations of inflammatory cytokines were calculated for each cornea.

Statistics

GraphPad Prism software version 10.1.1 for macOS (GraphPad software Inc., Boston, MA, USA) was used to process the data. At least three samples were tested for each experiment, and data were presented as means ± SD. In the statistical analysis, a Student's *t* test was used to assess differences between two groups. Statistical comparison was performed using a one-way analysis of variance (ANOVA) multigrouped point data and two-way ANOVA followed by Tukey's post hoc test for multi–time point longitudinal data. A value of $P < 0.05$ was considered statistically significant ($^{*}P < 0.05$, $^{**}P < 0.01$, $^{***}P < 0.001$, and $^{****}P < 0.0001$; ns, no significance). ImageJ software version 2.1.0 for macOS (ImageJ, MD, USA) was used to analyze images.

Supplementary Materials

The PDF file includes:

Figs. S1 to S11

Legend for movie S1

Other Supplementary Material for this manuscript includes the following:

Movie S1

REFERENCES AND NOTES

1. C. L. Bourlais, L. Acar, H. Zia, P. A. Sado, T. Needham, R. Leverge, Ophthalmic drug delivery systems—Recent advances. *Prog. Retin. Eye Res.* **17**, 33–58 (1998).
2. R. Langer, New methods of drug delivery. *Science* **249**, 1527–1533 (1990).
3. C. Wang, Y. Pang, Nano-based eye drop: Topical and noninvasive therapy for ocular diseases. *Adv. Drug Deliv. Rev.* **194**, 114721 (2023).
4. B. Grassiri, Y. Zambito, A. Bernkop-Schnürch, Strategies to prolong the residence time of drug delivery systems on ocular surface. *Adv. Colloid Interface Sci.* **288**, 102342 (2021).
5. C. E. Hamill, S. Bozorg, H. Y. P. Chang, H. Lee, R. R. Sayegh, A. N. Shukla, J. Chodosh, Corneal alkali burns: a review of the literature and proposed protocol for evaluation and treatment. *Int. Ophthalmol. Clin.* **53**, 185–194 (2013).
6. L. Quaranta, A. Novella, M. Tettamanti, L. Pasina, R. N. Weinreb, A. Nobili, Adherence and persistence to medical therapy in glaucoma: An overview. *Ophthalmol. Ther.* **12**, 2227–2240 (2023).
7. A. Urtti, Challenges and obstacles of ocular pharmacokinetics and drug delivery. *Adv. Drug Deliv. Rev.* **58**, 1131–1135 (2006).
8. C. Baudouin, A. Labbé, H. Liang, A. Pauly, F. Brignole-Baudouin, Preservatives in eyedrops: The good, the bad and the ugly. *Prog. Retin. Eye Res.* **29**, 312–334 (2010).
9. M. Yang, W. Xu, Z. Chen, M. Chen, X. Zhang, H. He, Y. Wu, X. Chen, T. Zhang, M. Yan, J. Bai, C. McAlinden, K. M. Meek, J. Yu, S. Ding, R. Gao, J. Huang, X. Zhou, Engineering hibiscus-like Riboflavin/ZIF-8 microsphere composites to enhance transepithelial corneal cross-linking. *Adv. Mater.* **34**, e2109865 (2022).
10. Y. Tian, T. Zhang, J. Li, Y. Tao, Advances in development of exosomes for ophthalmic therapeutics. *Adv. Drug Deliv. Rev.* **199**, 114899 (2023).
11. A. Than, C. Liu, H. Chang, P. K. Duong, C. M. G. Cheung, C. Xu, X. Wang, P. Chen, Self-implantable double-layered micro-drug-reservoirs for efficient and controlled ocular drug delivery. *Nat. Commun.* **9**, 4433 (2018).
12. S. Li, Z. Lu, Y. Huang, Y. Wang, Q. Jin, X. Shentu, J. Ye, J. Ji, K. Yao, H. Han, Anti-oxidative and anti-inflammatory micelles: Break the dry eye vicious cycle. *Adv. Sci.* **9**, 2200435 (2022).
13. C. J. Yang, D. D. Nguyen, J. Y. Lai, Poly (l-Histidine)-mediated on-demand therapeutic delivery of roughened ceria nanocages for treatment of chemical eye injury. *Adv. Sci.* **10**, 2302174 (2023).
14. Y. Zhang, C. Li, Q. Zhu, R. Liang, C. Xie, S. Zhang, Y. Hong, H. Ouyang, A long-term retaining molecular coating for corneal regeneration. *Bioact. Mater.* **6**, 4447–4454 (2021).
15. G. Trujillo-de Santiago, R. Sharifi, K. Yue, E. S. Sani, S. S. Kashaf, M. M. Alvarez, J. Leijten, A. Khademhosseini, R. Dana, N. Annabi, Ocular adhesives: Design, chemistry, crosslinking mechanisms, and applications. *Biomaterials* **197**, 345–367 (2019).
16. W. Hou, J. Li, Z. Cao, S. Lin, C. Pan, Y. Pang, J. Liu, Decorating bacteria with a therapeutic nanocoating for synergistically enhanced biotherapy. *Small* **17**, e2101810 (2021).
17. J. M. Porth, E. Deiotte, M. Dunn, R. Bashshur, A review of the literature on the global epidemiology of corneal blindness. *Cornea* **38**, 1602–1609 (2019).
18. S. R. Flaxman, R. R. A. Bourne, S. Resnikoff, P. Ackland, T. Braithwaite, M. V. Cicinelli, A. Das, J. B. Jonas, J. Keeffe, J. H. Kempen, J. Leasher, H. Limburg, K. Naidoo, K. Pesudovs, A. Silvester, G. A. Stevens, N. Tahhan, T. Y. Wong, H. R. Taylor, Vision Loss Expert Group of the Global Burden of Disease Study, Global causes of blindness and distance vision impairment 1990–2020: A systematic review and meta-analysis. *Lancet Glob. Health* **5**, e1221–e1234 (2017).
19. M. Ziaei, C. Greene, C. R. Green, Wound healing in the eye: Therapeutic prospects. *Adv. Drug Deliv. Rev.* **126**, 162–176 (2018).
20. J. P. Whitcher, M. Srinivasan, M. P. Upadhyay, Corneal blindness: A global perspective. *Bull. W. H. O.* **79**, 214–221 (2001).
21. C. Kaewsaneha, P. Tangboriboonrat, D. Polpanich, M. Eissa, A. Elaissari, Janus colloidal particles: Preparation, properties, and biomedical applications. *ACS Appl. Mater. Interfaces* **5**, 1857–1869 (2013).
22. C. Cui, T. Wu, X. Chen, Y. Liu, Y. Li, Z. Xu, C. Fan, W. Liu, A janus hydrogel wet adhesive for internal tissue repair and anti-postoperative adhesion. *Adv. Funct. Mater.* **30**, 2005689 (2020).
23. W. Liang, W. He, R. Huang, Y. Tang, S. Li, B. Zheng, Y. Lin, Y. Lu, H. Wang, D. Wu, Peritoneum-inspired Janus porous hydrogel with anti-deformation, anti-adhesion, and pro-healing characteristics for abdominal wall defect treatment. *Adv. Mater.* **34**, e2108992 (2022).
24. Y. He, Q. Li, P. Chen, Q. Duan, J. Zhan, X. Cai, L. Wang, H. Hou, X. Qiu, A smart adhesive Janus hydrogel for non-invasive cardiac repair and tissue adhesion prevention. *Nat. Commun.* **13**, 7666 (2022).
25. B. R. Freedman, A. Kuttler, N. Beckmann, S. Nam, D. Kent, M. Schuleit, F. Ramazani, N. Accart, A. Rock, J. Li, M. Kurz, A. Fisch, T. Ullrich, M. W. Hast, Y. Tinguely, E. Weber, D. J. Mooney, Enhanced tendon healing by a tough hydrogel with an adhesive side and high drug-loading capacity. *Nat. Biomed. Eng.* **6**, 1167–1179 (2022).
26. Y. Wang, Y. Sun, A. J. Avestro, P. R. McGonigal, H. Zhang, Supramolecular repair of hydration lubrication surfaces. *Chem* **8**, 480–493 (2022).
27. Q. Yue, L. Lei, Y. Gu, R. Chen, M. Zhang, H. Yu, S. Li, L. Yang, Y. Zhang, X. Zhao, Bioinspired polysaccharide-derived zwitterionic brush-like copolymer as an injectable biolubricant for arthritis treatment. *Adv. Healthc. Mater.* **11**, e2200090 (2022).
28. H. Fan, L. Wang, X. Feng, Y. Bu, D. Wu, Z. Jin, Supramolecular hydrogel formation based on tannic acid. *Macromolecules* **50**, 666–676 (2017).
29. H. Ejima, J. J. Richardson, K. Liang, J. P. Best, M. P. van Koeverden, G. K. Such, J. Cui, F. Caruso, One-step assembly of coordination complexes for versatile film and particle engineering. *Science* **341**, 154–157 (2013).
30. Q. Li, C. Wen, J. Yang, X. Zhou, Y. Zhu, J. Zheng, G. Cheng, J. Bai, T. Xu, J. Ji, S. Jiang, L. Zhang, P. Zhang, Zwitterionic biomaterials. *Chem. Rev.* **122**, 17073–17154 (2022).
31. W. Lin, J. Klein, Control of surface forces through hydrated boundary layers. *Curr. Opin. Colloid Interface Sci.* **44**, 94–106 (2019).
32. Z. Meng, Y. Jiao, P. Wu, Alleviating side reactions on Zn anodes for aqueous batteries by a cell membrane derived phosphorylcholine zwitterionic protective layer. *Angew. Chem. Int. Ed. Engl.* **135**, e202307271 (2023).
33. R. C. Nagarwal, S. Kant, P. N. Singh, P. Maiti, J. K. Pandit, Polymeric nanoparticulate system: A potential approach for ocular drug delivery. *J. Control. Release* **136**, 2–13 (2009).
34. F. Bian, F. S. A. Pelegrino, J. T. Henriksson, S. C. Pflugfelder, E. A. Volpe, D.-Q. Li, C. S. de Paiva, Differential effects of dexamethasone and doxycycline on inflammation and MMP production in murine alkali-burned corneas associated with dry eye. *Ocul. Surf.* **14**, 242–254 (2016).

35. M. Fujihara, M. Muroi, K.-i. Tanamoto, T. Suzuki, H. Azuma, H. Ikeda, Molecular mechanisms of macrophage activation and deactivation by lipopolysaccharide: Roles of the receptor complex. *Pharmacol. Ther.* **100**, 171–194 (2003).
36. X. Li, X. Jin, J. Wang, X. Li, H. Zhang, Dexamethasone attenuates dry eye-induced pyroptosis by regulating the KCNQ1OT1/miR-214 cascade. *Steroids* **186**, 109073 (2022).
37. D. Song, J. Zhao, W. Deng, Y. Liao, X. Hong, J. Hou, Tannic acid inhibits NLRP3 inflammasome-mediated IL-1β production via blocking NF-κB signaling in macrophages. *Biochem. Biophys. Res. Commun.* **4**, 3078–3085 (2018).
38. M. Kobyakova, Y. Lomovskaya, A. Senotov, A. Lomovsky, V. Minaychev, I. Fadeeva, D. Shtatnova, K. Krasnov, A. Zvyagina, I. Odinokova, V. Akatov, R. Fadeev, The increase in the drug resistance of acute myeloid leukemia THP-1 cells in high-density cell culture is associated with inflammatory-like activation and anti-apoptotic Bcl-2 proteins. *Int. J. Mol. Sci.* **23**, 7881 (2022).
39. Z. Xue, J. Zeng, Y. Li, B. Meng, X. Gong, Y. Zhao, X. Dai, Proteomics reveals that cell density could affect the efficacy of drug treatment. *Biochem. Biophys. Rep.* **33**, 101403 (2022).
40. S. Krishnaiah, P. K. Nirmalan, B. R. Shamanna, M. Srinivas, G. N. Rao, R. Thomas, Ocular trauma in a rural population of southern India: The Andhra Pradesh eye disease study. *Ophthalmology* **113**, 1159–1164 (2006).
41. S. A. Eming, T. A. Wynn, P. Martin, Inflammation and metabolism in tissue repair and regeneration. *Science* **356**, 1026–1030 (2017).
42. R. Medzhitov, Origin and physiological roles of inflammation. *Nature* **454**, 428–435 (2008).
43. B. Shukla, R. Agrawal, D. Shukla, S. Seen, Systematic analysis of ocular trauma by a new proposed ocular trauma classification. *Indian J. Ophthalmol.* **65**, 719–722 (2017).
44. S. E. Wilson, L. P. Sampaio, T. M. Shiju, G. S. Hilgert, R. C. de Oliveira, Corneal opacity: Cell biological determinants of the transition from transparency to transient haze to scarring fibrosis, and resolution, after injury. *Invest. Ophthalmol. Vis. Sci.* **63**, 22 (2022).
45. A. A. Ahmmed, D. S. J. Ting, F. C. Figueiredo, Epidemiology, economic and humanistic burdens of ocular surface chemical injury: A narrative review. *Ocul. Surf.* **20**, 199–211 (2021).
46. N. Sharma, M. Kaur, T. Agarwal, V. S. Sangwan, R. B. Vajpayee, Treatment of acute ocular chemical burns. *Surv. Ophthalmol.* **63**, 214–235 (2018).
47. X. Shi, T. Zhou, S. Huang, Y. Yao, P. Xu, S. Hu, C. Tu, W. Yin, C. Gao, J. Ye, An electrospun scaffold functionalized with a ROS-scavenging hydrogel stimulates ocular wound healing. *Acta Biomater.* **158**, 266–280 (2023).
48. H. S. Dua, D. S. J. Ting, A. Al Saadi, D. G. Said, Chemical eye injury: Pathophysiology, assessment and management. *Eye* **34**, 2001–2019 (2020).
49. Y. Gong, D.-R. Koh, Neutrophils promote inflammatory angiogenesis via release of preformed VEGF in an in vivo corneal model. *J. Cell Tissue Res.* **339**, 437–448 (2010).
50. A. H. Paes, A. Bakker, C. J. Soe-Agnie, Impact of dosage frequency on patient compliance. *Diabetes Care* **20**, 1512–1517 (1997).
51. N. H. Bennett, H. R. Chinnery, L. E. Downie, L. J. Hill, L. M. Grover, Material, immunological, and practical perspectives on eye drop formulation. *Adv. Funct. Mater.* **30**, 1908476 (2020).
52. B. Barrientez, S. E. Nicholas, A. Whelchel, R. Sharif, J. Hjortdal, D. Karamichos, Corneal injury: Clinical and molecular aspects. *Exp. Eye Res.* **186**, 107709 (2019).
53. S. S. Chaurasia, R. R. Lim, R. Lakshminarayanan, R. R. Mohan, Nanomedicine approaches for corneal diseases. *J. Funct. Biomater.* **6**, 277–298 (2015).
54. A. V. Ljubimov, M. Saghizadeh, Progress in corneal wound healing. *Prog. Retin. Eye Res.* **49**, 17–45 (2015).
55. D. Roshandel, M. Eslani, A. Baradaran-Rafii, A. Y. Cheung, K. Kurji, S. Jabbehdari, A. Maiz, S. Jalali, A. R. Djalilian, E. J. Holland, Current and emerging therapies for corneal neovascularization. *Ocul. Surf.* **16**, 398–414 (2018).
56. Z. Li, J. Jiang, K. Chen, Q. Chen, Q. Zheng, X. Liu, H. Weng, S. Wu, W. Chen, Preventing corneal blindness caused by keratitis using artificial intelligence. *Nat. Commun.* **12**, 3738 (2021).
57. K. H. Hung, L. K. Yeh, Ex vivo and in vivo animal models for mechanical and chemical injuries of corneal epithelium. *J. Vis. Exp.* **182**, e63217 (2022).
58. V. Villabona-Martinez, L. P. Sampaio, T. M. Shiju, S. E. Wilson, Standardization of corneal alkali burn methodology in rabbits. *Exp. Eye Res.* **230**, 109443 (2023).

Acknowledgments: Figures 1, B and C and 3E were created in BioRender [C.W. (2025); https://BioRender.com/k75b731]. **Funding:** This work was supported by the National Natural Science Foundation of China (22375127 to Y.P., 22475131 to F.W., and 82388101 to X.F.), the Shanghai Rising-Star Program (23QA1408600 to F.W.), the Foundation of National Infrastructures for Translational Medicine (Shanghai) (TMSK-2021-123 to Y.P.), the Innovative Research Team of High-level Local Universities in Shanghai (SHSMU-ZDCX20210700 to Y.P.), the Innovative Research Team of High-level Local Universities in Shanghai (SHSMU-ZDCX20210900 to X.F.), the Science and Technology Commission of Shanghai Municipality (20DZ22780800 to X.F.), the Shanghai Key Clinical Specialty, Shanghai Eye Disease Research Center (2022ZZ01003 to X.F.), Shanghai Frontiers Science Center of Drug Target Identification and Delivery (ZXWH2170101/030 to Y.P.), and the startup funding from Shanghai Jiao Tong University (Y.P.). **Author contributions:** Conceptualization: Y.P., X.F., F.W., and X.K. Investigation: C.W., X.L., W.L., and X.K. Methodology: C.W., X.L., X.K., F.W., and Y.P. Validation: C.W., X.L., W.L., and X.K. Visualization: C.W., X.K., and F.W. Data analysis: C.W., X.L., X.K., and F.W. Writing—original draft: C.W., X.L., F.W., and Y.P. Writing—review and editing: F.W., X.F., and Y.P. Supervision: F.W., X.F., and Y.P. **Competing interests:** X.F., Y.P., and C.W. have applied for a patent (202411242421.5) from the State Intellectual Property Office (China). The authors declare that they have no other competing interests. **Data and materials availability:** All data needed to evaluate the conclusions in the paper are present in the paper and/or the Supplementary Materials.

Submitted 26 July 2024
Accepted 3 February 2025
Published 7 March 2025
10.1126/sciadv.ads0282